minerals

MDPI

Article

Assessing the Ion Adsorption REE Potential of Weathered Granite Profiles on Bangka Island, Indonesia: Mineralogical, Geochemical, and Geomorphological Evidence

Periska Rasma [1], Syafrizal [2,*], Arie Naftali Hawu Hede [2], Andy Yahya Al Hakim [2], Iwan Setiawan [3] and I Gde Sukadana [4]

[1] Doctoral Program in Mining Engineering, Faculty of Mining and Petroleum Engineering, Institut Teknologi Bandung, Bandung 40132, Indonesia; periskarasma@gmail.com
[2] Earth Resources Exploration Research Group, Faculty of Mining and Petroleum Engineering, Institut Teknologi Bandung, Bandung 40132, Indonesia; ariehede@itb.ac.id (A.N.H.H.); andyyahya@itb.ac.id (A.Y.A.H.)
[3] Research Center for Geological Resources, National Research and Innovation Agency, Bandung 40135, Indonesia; iwan027@brin.go.id
[4] Research Center for Nuclear Material and Radioactive Waste Technology, National Research and Innovation Agency, South Tangerang 15314, Indonesia; igde001@brin.go.id
* Correspondence: syafrizal@itb.ac.id

Abstract

Ion-adsorption deposits hosted in weathered granites are the main source of rare earth elements (REE) produced in Southeast Asia, and Indonesia, with the same granitic lithology and tropical climate, has comparable potential. However, the processes that concentrate REE in such deposits, particularly the influence of topography, remain incompletely understood. This study investigated the mineralogical, geochemical, and geomorphological controls on REE mobility and enrichment in weathered granite profiles on Bangka Island, Indonesia. Thirty-nine samples, comprising six fresh granites and 33 weathered samples from eight profiles spanning flat to hilly slopes, were analyzed using petrography, X-ray diffraction, scanning electron microscopy with energy-dispersive spectroscopy (SEM–EDS), micro-X-ray fluorescence, and whole-rock geochemistry. SEM–EDS identifies monazite-(Ce), allanite-(Ce), zircon, and apatite as REE-bearing minerals in the parent granites. Enrichment is strongest, up to ~575 ppm total REE and yttrium (~0.07 wt.% total rare earth oxides), in the B horizon of a profile on a moderate (8%–15%) slope, whereas hilly profiles are erosion-affected and flat lowland profiles show limited enrichment. Enrichment reflects parent-rock mineralogy, redox-controlled Ce behavior, and slope stability. These indicators provide initial screening guides for ion-adsorption REE exploration in tropical granitic terrains, to be refined by quantifying the ion-exchangeable REE fraction and regolith REE hosts.

Keywords: rare earth elements; ion adsorption deposits; weathered granite; geomorphology; Bangka Island

Academic Editor: Harald G. Dill

Received: 8 October 2026
Revised: 17 November 2026
Accepted: 24 November 2026
Published: 27 November 2026

Copyright: © 2026 by the authors. Licensee MDPI, Basel, Switzerland. This article is an open access article distributed under the terms and conditions of the Creative Commons Attribution (CC BY) license.

1. Introduction

Rare earth elements (REE) comprise 17 elements, conventionally split into the light (LREE) and heavy (HREE) subgroups [1]. In the continental crust, HREE are considerably less abundant than LREE [2]. REE are essential for numerous advanced technologies,

including renewable energy systems, electronics, and defense applications [1]. Due to rapidly increasing global demand and limited diversity of supply sources, understanding the geological processes controlling REE enrichment and mobility has become increasingly critical [3]. Most economically viable REE deposits occur in carbonatites, alkaline complexes, and placer deposits; however, ion adsorption REE deposits derived from weathering of granitic rocks are gaining interest due to their economic viability, simpler processing methods, and lower environmental impacts [4,5].

Chemical weathering drives the formation of ion-adsorption REE deposits by breaking down REE-bearing minerals and releasing REE into the solution [4]. The mobility and subsequent enrichment of these REE depend significantly on local chemical environments—particularly leaching intensity, pH conditions, and the presence of secondary clay minerals like kaolinite, and Fe/Al oxides, which effectively adsorb REE [6]. The major deposits occur in southern China, where intense tropical weathering of granites has produced REE-rich lateritic regoliths [7,8]. Similar systems are also found in Madagascar [9], in regolith-hosted deposits of Western Australia [10], and elsewhere in Southeast Asia in lateritic nickel and bauxite deposits [11–14].

Bangka Island hosts extensive weathered granite profiles, making it a promising yet under-investigated region for ion adsorption REE deposits [11,15]. In addition, the tropical climate—with its high annual rainfall and temperatures—accelerates chemical weathering and favors the development of ion adsorption REE deposits [16]. Previous research indicates that weathering intensity, topography, and mineralogical and geochemical compositions significantly influence REE mobility and enrichment [17–21].

Even with this general understanding, exactly how topography controls REE mobility in tropical terrains, including Bangka Island, remains poorly understood. Because most of the existing literature focuses on mineralogical and geochemical analyses, a clear knowledge gap remains regarding how slope dynamics influence the vertical distribution and enrichment of REE. By integrating mineralogical, geochemical, and geomorphological analyses, this study provides new insights into REE mobility and enrichment processes in tropical granitic terrains and contributes to improved exploration strategies for regolith-hosted ion adsorption REE deposits.

2. Geological Settings

Bangka Island lies within the Southeast Asian Tin Belt, an extensive Paleozoic–Mesozoic metallogenic province whose evolution is tied to the closure of the Paleo-Tethys Ocean [15]. The belt is well known for hosting major granitoid-related tin and REE mineralization. Recently, the Bangka granites have been interpreted as biotite granite and hornblende–biotite granite, crustally derived melts generated by partial melting of older metasedimentary rocks [22,23]. In the field, granite rocks are frequently linked to cassiterite-bearing and greisen systems [15,23].

The geological map of the study area (Figure 1) provides a detailed overview of five main lithological units and the sampling locations (B1–B8). The Tanjunggenting Formation (TRt) dominates the central and southern sectors of the island and consists of thick metasedimentary and volcaniclastic sequences. Meanwhile, the Klabat Granite (TRJkg) extends across most of the study area and consists of a widely distributed peraluminous S-type granite complex, cropping out mainly in the northern and southern parts of the island. Toward the east–northeast, the geological formations evolved into exposed rock outcrops that were spread out. These include metamorphic rocks of the Pemali Complex (CPp) and younger sedimentary beds of the Rangam Formation (TQr). In addition, Quaternary alluvial deposits (Qa) cover the river valleys and coastal plains; these unconsolidated sediments have been the primary target of extensive alluvial tin mining operations [24,25].

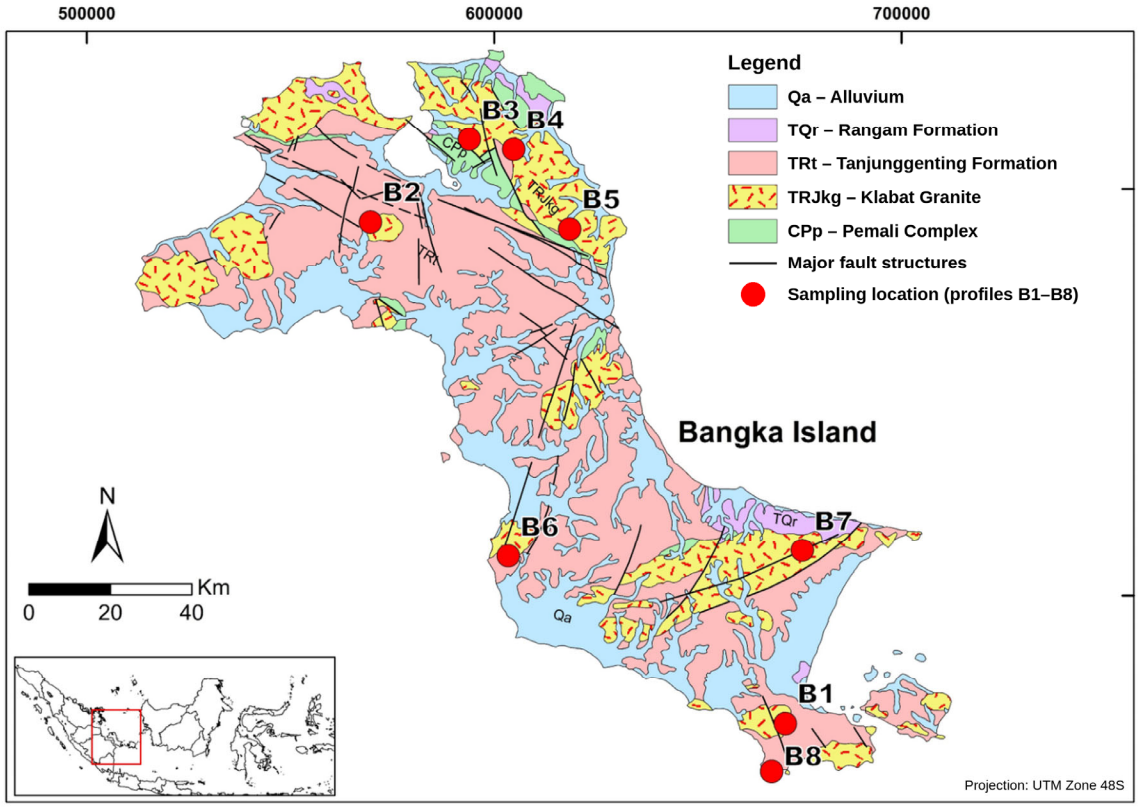


Figure 1. Geological map of Bangka Island showing the main lithological units, the major fault structures, and the locations of the eight weathered granite profiles (B1–B8), compiled from the regional geological maps [24,25]. Coordinates are in UTM Zone 48S; the inset shows the location of the study area (red box) in Indonesia.

Based on U–Pb dating of cassiterite, the granite intrusions associated with tin mineralization on Bangka Island formed primarily during the Late Triassic period, between 230 and 210 Ma. This period aligns with the metallogenic ages recorded in the Main Range tin belt in Malaysia and Thailand [26]. Texturally, these granites are medium- to coarse-grained, with quartz, K-feldspar, plagioclase, and biotite as their main minerals [22]. They also carry REE-bearing minerals such as monazite, xenotime, zircon, and apatite [27,28]. The granitic magma intruded into older metasedimentary units and has since developed extensive weathering profiles, which are especially prominent across the central and southern parts of the island [29,30]. Figure 2 shows representative field exposures of these granites and the weathered profiles developed on them at the sampling localities.

The landscape of Bangka Island is relatively flat, with gentle hills and low- to medium-height ridges, with the highest point reaching around 705 meters at Mount Maras. Under a tropical climate, the study area experiences intense chemical weathering of the granitic bedrock, with average temperatures of around 27 °C and annual rainfall reaching up to 3000 mm [31,32]. These conditions produce thick regolith profiles enriched in secondary minerals such as kaolinite, gibbsite, and Fe–Al oxides [33]. From a mineralogical perspective, the REE-bearing minerals in these granites (primarily monazite and xenotime) are relatively resistant but partly break down under intense tropical weathering [29,30]. Once released, the REE are not simply carried away by runoff; rather, they can be captured and preserved through adsorption onto clay minerals, most of which are deposited within the B horizon of the saprolite zone [34–36].

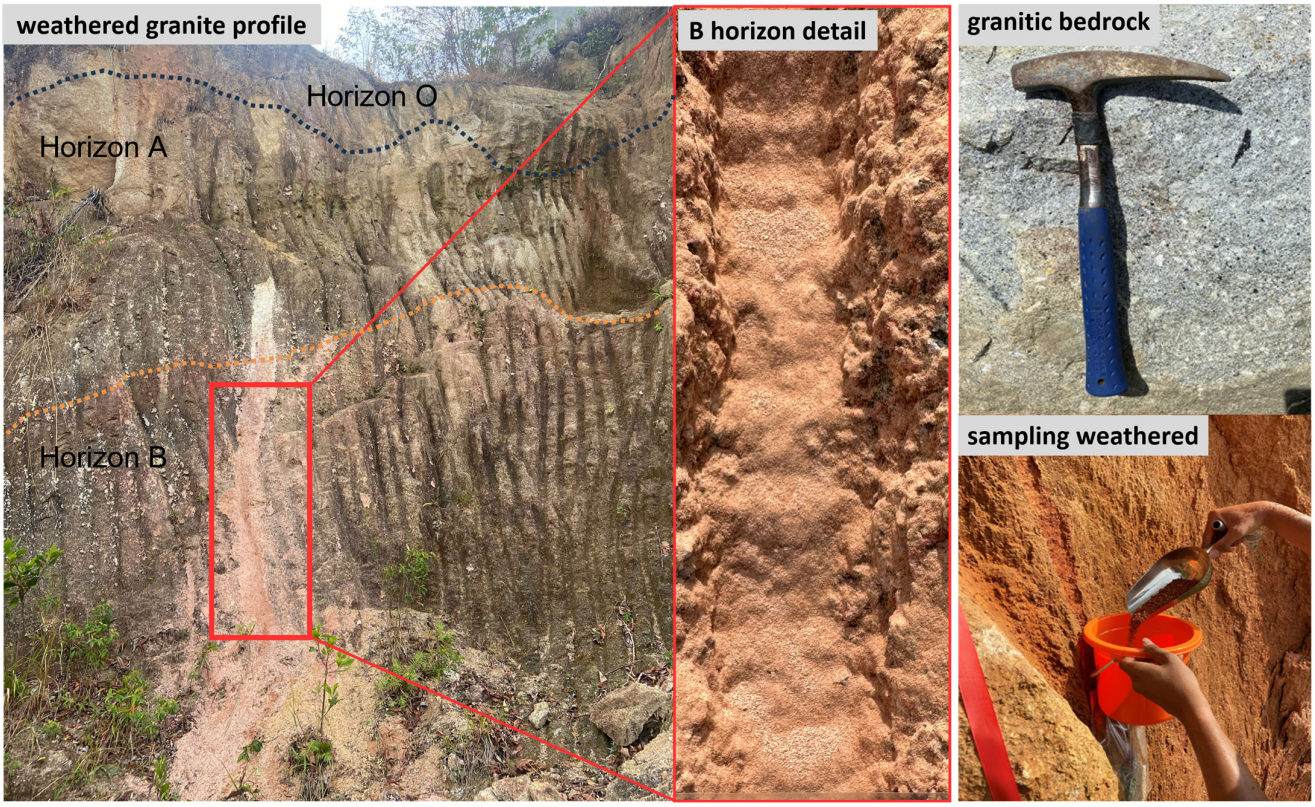


Figure 2. Field photographs of representative granite exposures and weathered granite profiles at the sampling localities on Bangka Island.

3. Materials and Methods

The following subsections outline the sampling strategy, the mineralogical observations, the geochemical analyses, and the terrain analysis carried out in this study.

3.1. Samples and Classification of Sampling Locations

To determine mineralogical and geochemical variations with depth, this study collected 39 samples—6 fresh granite samples and 33 weathered samples—from eight weathered granite profiles (B1–B8) distributed across Bangka Island (Figure 1). The vertical channel sampling method ensured representative depth profiles covering all horizons. The exposed regolith profiles studied here range from approximately 2.3 to 7.9 m thick, and the depth intervals of their weathering horizons are given in Table 1. Most profiles exhibit four classic horizons: an organic-rich topsoil layer (O horizon); a highly weathered A horizon rich in secondary clay; a partially weathered B horizon that still preserves some of the original granite texture; and, below, the parent bedrock (C horizon) [33].

Site selection intentionally targeted a wide range of weathering intensities and topographic landscapes. By categorizing these profiles by relative elevation and slope gradient, the analysis could better assess how local topography drives both weathering and REE mobilization. Moreover, all profiles were developed on granitoids from the same Late Triassic Bangka suite under a uniform equatorial climate, which constrains—though does not fully remove—lithological and climatic variability among sites. The relative elevation, expressed as the percentage of the sampling elevation relative to the height of the nearest local peak, is divided into five zones: top hill (>80% of local peak height), uphill (50%–80%), downhill (25%–50%), foothill (8%–25%), and lowland (0%–8%). For slope gradients, the framework adopted a classification scheme simplified from USDA guidelines [37]:

steep (30%–65%), hilly (15%–30%), moderate (8%–15%), and flat (<8%). Notably, the sampling excluded top-hill and steep-slope environments; these areas were either physically inaccessible or lacked well-exposed weathered granite profiles.

Table 1 provides a detailed breakdown of how each specific site fits into these geomorphological parameters. For example, site B5 (Bukit Siam) falls into the hilly slope classification; it sits at 64 meters above sea level (masl)—representing 53.3% of the local 120 m peak—and has a 21.3% gradient. In contrast, the sampling points at B6 (Bukit Permis) and B1 (Bukit Muntai) fall within the moderate slope category. Although their absolute elevations reach 91 masl and 80 masl, their gradients drop below 10%, resulting in much lower relative elevations (18.6% and 27.6%, respectively), which place B6 in the foothill zone and B1 in the downhill zone. Further down, sites B7 and B8, positioned near Bukit Pading and Bukit Namak, also fall into the foothill category but have flat slopes and minimal elevation shifts. In addition, sites B2, B3, and B4 lie on flat lowlands below 50 masl, with no well-defined hilltop reference points. These lowland locations record the most advanced weathering observed in this study, and the unaltered parent rock of the C horizon is completely missing.

Table 1. Classification of sampling locations based on elevation and slope gradient, including their geographical categories and slope types [37], and the parent rock and depth intervals of the weathering horizons of each profile.

No	Code of Sample Locations	Sampling Elevation (masl)	Highest Peak of Nearest Hill (masl)	Elevation from the Highest Peak (%)	Slope Gradient (%)	Categorical of Sampling Location	Slope Classifications
1	B1	80	290	27.6	8.3	Downhills	Moderate
2	B2	18	-	-	6.0	Lowlands	Flat
3	B3	49	-	-	2.5	Lowlands	Flat
4	B4	35	-	-	1.1	Lowlands	Flat
5	B5	64	120	53.3	21.3	Uphills	Hilly
6	B6	91	490	18.6	9.17	Foothills	Moderate
7	B7	70	650	10.8	3.1	Foothills	Flat
8	B8	15	127	11.8	1.8	Foothills	Flat

Parent rock and weathering horizons of each profile

No	Code of sample locations	Parent rock (C horizon)	Exposed thickness (m)	O horizon depth (m)	A horizon depth (m)	B horizon depth (m)
1	B1	Biotite granite (B1-R)	6.0	0–0.4	0.4–3.0	3.0–5.0
2	B2	Not exposed; Klabat Granite inferred	2.3	0–0.3	0.3–0.8	0.8–2.3
3	B3	Not exposed; Klabat Granite inferred	7.9	0–0.3	0.3–6.0	6.0–7.9
4	B4	Not exposed; Klabat Granite inferred	5.0	Absent	0–3.0	3.0–5.0
5	B5	Biotite granite (B5-R)	6.8	0–0.7	0.7–2.7	2.7–6.5
6	B6	Biotite granite (B6-R2); tourmalinized granite (B6-R1)	4.0	0–0.8	0.8–1.6	1.6–3.8
7	B7	Biotite granite (B7-R)	4.0	0–0.4	0.4–2.0	2.0–4.0
8	B8	Hornblende–biotite granite (B8-R)	3.0	0–0.6	0.6–1.3	1.3–2.5

Depths are given from the ground surface (top–bottom); absent = horizon not developed. Parent-rock names are based on petrography. The Klabat Granite (TRJkg) is inferred for profiles B2–B4 from the regional geological maps [24,25].

Among the eight profiles, five sites (B1, B5, B6, B7, and B8) display complete weathering sequences, thereby enabling a comprehensive assessment of vertical geochemical and mineralogical transformations. Meanwhile, sites B2, B3, and B4 have no preserved C horizon, as the fresh granite has been removed by erosion in the lowland areas. Fresh granite samples (R) were collected from the C horizon to represent the mineralogical and geochemical baselines, whereas weathered samples (S) were obtained from the O, A, and B horizons to capture progressive changes due to weathering.

3.2. Mineralogical Observations

For the initial characterization, petrographic analyses utilized a Nikon LV100N optical microscope (Nikon Corporation, Tokyo, Japan) at Institut Teknologi Bandung (ITB). Preparing thin sections from representative fresh granite specimens allowed detailed observation of primary rock-forming and accessory minerals, mapping of textural relationships, and identification of potential REE-bearing minerals. For the QAP classification, the modal proportions of quartz, alkali feldspar, and plagioclase were estimated visually in six fields of view per thin section; the six estimates were averaged and recalculated to Q + A + P = 100. Establishing this qualitative baseline proved crucial, as it directly guided the final selection of samples for more in-depth mineralogical and geochemical testing.

To identify and quantify the specific mineral phases in the chosen samples, subsequent testing used X-ray diffraction (XRD) on a Rigaku SmartLab diffractometer (Rigaku Corporation, Tokyo, Japan) also housed at ITB. This specific analytical step was heavily relied upon due to the instrument's high precision in detecting and quantifying clay minerals—the exact components that are absolutely essential for the formation of ion-adsorption REE deposits. Dried rock samples were ground into fine powder using an agate mortar, mounted in sample holders, and scanned over a 2θ range of 2–65° at a scanning rate of 2° per minute. Mineral phases were identified using Rigaku PDXL software (version 2.8, Rigaku Corporation, Tokyo, Japan) in conjunction with the International Centre for Diffraction Data (ICDD) database. Background noise was reduced, and peak resolution improved using Fityk freeware to enhance analytical accuracy [38].

The polished thin sections were then examined on a JEOL JSM-6510LA scanning electron microscope (SEM) (JEOL Ltd., Akishima, Tokyo, Japan) equipped with a JEOL JED-2300 energy-dispersive X-ray spectrometer (EDS), run at 15 kV accelerating voltage and a probe current of 7.475×10^{-9} A, with a live time of 50 s per EDS spectrum. Images were recorded in secondary-electron (SEI) mode, and the REE- and Th-bearing accessory grains were identified by EDS spot analyses. Semi-quantitative element concentrations were obtained by standardless ZAF correction and normalized to 100 wt.% (Supplementary S1). These data are used for mineral identification only, because overlaps among the REE L-lines limit the accuracy of individual REE concentrations; electron-probe microanalysis (EPMA) was not available. Because image contrast favors phases with a high mean atomic number (e.g., thorite, monazite, and zircon), REE carriers with weaker contrast, such as allanite and REE fluorocarbonates, may be under-represented in the SEM observations. To complement SEM observations, micro-X-ray fluorescence (μXRF) analysis was conducted using a Bruker M4 Tornado Plus instrument (Bruker Nano GmbH, Berlin, Germany) at the Center for Research and Technology of Nuclear Minerals, National Research and Innovation Agency, Indonesia. The μXRF system was operated at 50 kV and 600 μA, with a spot size of 20 μm and an acquisition time of 12–15 milliseconds per pixel, scanning areas of ≥4 cm^2 per sample. The resulting elemental maps were processed using the

Advanced Mineral Identification and Characterization System (AMICS), which enables mineral phase identification through spectral matching with its internal database.

The μXRF data were used only as a reconnaissance tool to visualize element distributions at the centimeter scale and to select areas for SEM–EDS examination. The nominal spot size of 20 μm increases at the lower energies of the REE L-lines, and the information depth of μXRF reaches tens to hundreds of micrometers for high-energy lines [39]. Because most REE-bearing accessory grains in the studied granites are <50 μm, and xenotime and zircon are commonly <20 μm, their spectra are mixed with those of the surrounding minerals. Spectral overlaps (e.g., Ba Lβ$_1$ and Ti Kβ with Ce Lα, Ce Lβ$_1$ with Nd Lα, and Rb Kβ with Y Kα) may also produce apparent REE signals. Therefore, the AMICS phase maps are considered indicative only for the coarse rock-forming minerals, and accessory minerals are identified exclusively by SEM–EDS.

3.3. Geochemical Analysis

Initial sample preparation involved drying all collected materials. The dried samples were pulverized until 95% of the material passed through a 200-mesh sieve, to achieve a particle size of <75 μm. This step is essential to ensure sample homogeneity and maintain analytical accuracy.

Major element oxide concentrations were determined by X-ray fluorescence (XRF) analysis of lithium borate fusion beads (FB1/XRF250), and loss on ignition (LOI) was measured by heating subsamples to 1000 °C to estimate volatile content—primarily H_2O and CO_2—associated with clay formation and mineral decomposition during chemical weathering. For this study, the XRF analyses were conducted using a MagiX FAST PANalytical instrument (PANalytical B.V., Almelo, The Netherlands).

Trace elements, including REE, were quantified by Agilent 7900 Inductively Coupled Plasma Mass Spectrometry (ICP-MS, Agilent Technologies, Inc., Santa Clara, CA, USA) following a rigorous four-acid digestion procedure (4A/MS11, Fisher Chemical, Thermo Fisher Scientific, Waltham, MA, USA). This protocol, employing hydrofluoric acid (HF), perchloric acid ($HClO_4$), nitric acid (HNO_3), and hydrochloric acid (HCl), ensures complete dissolution of silicate-rich matrices, including refractory phases in granitic rocks.

Both XRF and ICP-MS geochemical analyses in this study were conducted at PT Intertek Testing Services, a commercial laboratory that provides high-accuracy analytical services. The analytical uncertainty was estimated at ±0.5% for major oxides and ±0.01 ppm for trace elements, including REE.

The chemical index of alteration (CIA) and the aluminum saturation index (ASI) were calculated from molar proportions of the oxides [40]. TREY is reported as the sum of the lanthanides and Y; Sc is reported separately.

3.4. Terrain Analysis

The terrain of each profile was characterized by its altitude, relative elevation, slope gradient, and categorical sampling location (Section 3.1). Slope gradients were converted to slope angles (arctangent of the gradient), and the profiles were classified numerically by slope angle and altitude, following the approach of Dill et al. [41]. Each profile was assigned to a hillslope element and, on the basis of its landscape position, to one of the three hydrographic zones of a drainage system—the headwater, track, and deposition zones [41]. The two- and three-dimensional hydrographic parameters used in comparable terrain analyses [41] were derived from the Copernicus GLO-30 digital elevation model [42] at the profile coordinates recorded by handheld GPS during sampling. The DEM was reprojected to UTM Zone 48S at 30 m resolution. To make the channel positions follow the mapped rivers, the river lines of the 1:50,000 Rupabumi Indonesia (RBI) topographic map [43] (classes “Sungai” and “Sungai Satu Garis”) were burned 15 m into the DEM [44];

depressions were then filled, and D8 flow directions [45], flow accumulation, and a stream network (contributing area ≥ 1 km²) with Strahler orders [46] were computed with pysheds v0.5 (Python). All elevations, gradients, and heights were taken from the unmodified DEM. For each profile, we determined the drainage pattern around the site (2D), the order and catchment area of the receiving stream (the first stream reached along the flow path), the flow distance to that stream, the height above the nearest drainage (HAND) [47], and the local relief within a 1 km radius, and, along the receiving stream, the talweg gradient and the horizontal sinuosity (channel length divided by straight-line distance, measured on the D8 flow path smoothed with a 270 m moving average) over the first 2 km downstream and the number of knickpoints between the profile and the coast (3D). Knickpoints were defined as drops of ≥5 m over 300 m whose gradient exceeds three times that of the following 1 km, measured on talweg profiles from which positive vegetation artifacts were removed by taking the running minimum of the DEM downstream. Because GLO-30 is a surface model that includes vegetation, and the D8 network overestimates channel length at 30 m resolution, these parameters are used only for a relative comparison of the profiles. The receiving streams of six profiles coincide with mapped RBI rivers (within 25 m), the exception being B5, whose receiving stream is not mapped (B8 drains directly to the sea), and the DEM lies on average 3.5 m above the RBI contours (root-mean-square difference 8.8 m), consistent with the vegetation cover included in the surface model.

4. Results

This section presents the mineralogical and geochemical characteristics of the fresh granites and weathered granite profiles. The results are organized by mineralogical observations, followed by geochemical variations.

4.1. Mineralogical Variations in Fresh Granites

The mineralogical characteristics of the fresh granites were examined using complementary analytical techniques, including petrography, SEM–EDS characterization, μXRF mapping, and XRD analysis.

4.1.1. Petrographic Analysis

Under the microscope, the fresh granite samples are dominated by quartz, K-feldspar, plagioclase, and biotite, together with less than 1% accessory minerals—mainly ilmenite, apatite, zircon, and monazite; hornblende was identified only in B8-R. Biotite, part of which has been altered to chlorite, commonly encloses small (mostly <50 μm) accessory inclusions (Figure 3a), some of which are located at the center of dark pleochroic halos. These halos show that the inclusions contain radioactive elements (U and Th) and have caused radiation damage in the host biotite, but they do not identify the mineral species; the inclusions were therefore examined by SEM–EDS, and optical identifications of accessory minerals are regarded as provisional. A brownish, pleochroic phase resembling allanite occurs locally in B1-R (Figure 3b), and allanite-(Ce) was confirmed in this sample by SEM–EDS.

The feldspar minerals often exhibit a distinct perthitic texture accompanied by oscillatory zoning (Figure 3c), which represents typical geological evidence of slow magma cooling. The other samples show moderate alteration, particularly where Ca-rich plagioclase zones have undergone sericitization. One prominent feature is observed in sample B6-R2, which exhibits a distinctive, worm-like myrmekite texture (Figure 3d). This specific intergrowth highlights episodes of albitization and post-magmatic fluid alteration that likely influenced the local REE mineralization. Quartz remains the most abundant mineral overall, generally appearing as massive, optically clear grains. In localized patches,

however, it shifts into secondary microcrystalline quartz with noticeably curved grain boundaries (Figure 3e)—a clear fingerprint of post-magmatic recrystallization. Zircon also appears consistently throughout the matrix as a common REE-bearing mineral, typically restricted to tiny inclusions measuring less than 50 μm across, and in B8-R biotite is accompanied by hornblende (Figure 3f).

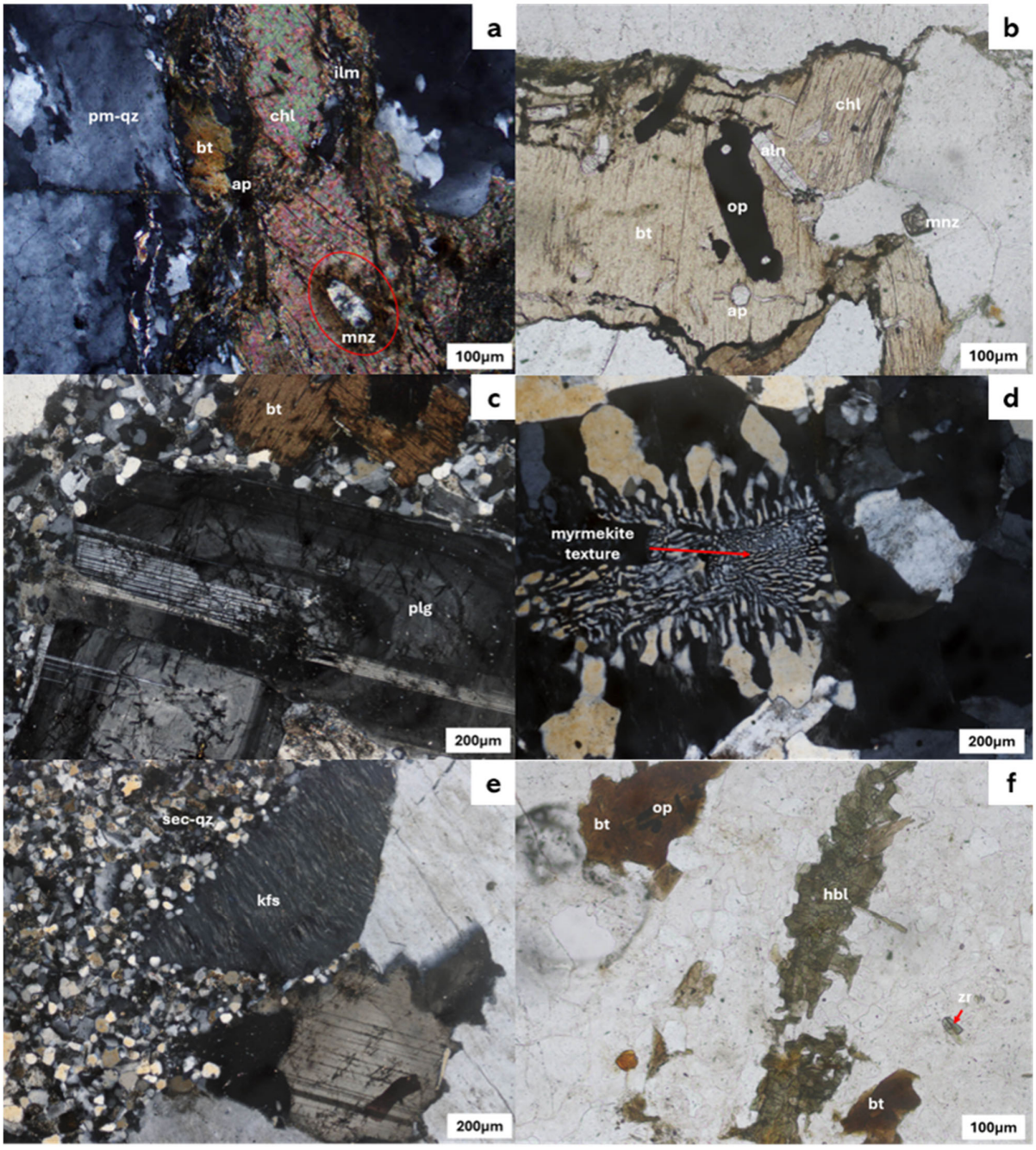


Figure 3. Photomicrographs of the fresh granite samples under the petrographic microscope. (**a**) B1-R: pleochroic halo around a radioactive (U–Th-bearing) accessory inclusion in biotite (XPL). (**b**) B1-R: apatite, monazite, and possible allanite as inclusions in biotite (PPL). (**c**) B5-R: oscillatory zoning in plagioclase, commonly altered in the core (XPL). (**d**) B6-R2: worm-like myrmekite texture (XPL). (**e**) B7-R: secondary quartz surrounding K-feldspar with perthite texture (XPL). (**f**) B8-R: biotite and hornblende grains (PPL). The red circle in (a) and the red arrows in (d) and (f) mark the monazite inclusion, the myrmekite intergrowth, and a zircon grain, respectively. Mineral abbreviations: Ilm

(ilmenite), Bt (biotite), Ap (apatite), Chl (chlorite), Mnz (monazite), Pm-Qz (primary quartz), Sec-Qz (secondary quartz), Plg (plagioclase), Kfs (K-feldspar), Hbl (hornblende), Op (opaque), Aln (allanite), Zr (zircon).

4.1.2. SEM–EDS Characterization of REE-Bearing Minerals

Representative SEM–EDS spot analyses of the REE- and Th-bearing accessory minerals, with the corresponding EDS spectra, are given in Supplementary S1, and SEM images of the analyzed grains are shown in Figure 4. In B1-R, a P-free spectrum with Si, Ca, Fe, and the light REE (Ce, Nd, La, and Pr) identifies allanite-(Ce) (Figure 4a). Monazite in B5-R yields spectra dominated by P, Ce, and La with minor Pr, consistent with monazite-(Ce) [$(Ce,La,Nd,Th)PO_4$], and forms irregular grains (Figure 4b); Nd and Th were not quantified because of peak overlaps. Thorite ($ThSiO_4$), characterized by Th–Si-dominated spectra, occurs in B1-R and as inclusions in apatite in B6-R1 (Figure 4a,c), whereas zircon in B5-R, B7-R, and B8-R gives Zr–Si spectra (Figure 4b,e,f). Apatite, confirmed by EDS in B7-R, occurs as coarse grains (Figure 4c) and as inclusions (<20 μm) in zircon (Figure 4d,e). Because the grains examined were not counted systematically, the frequency with which these minerals were observed does not represent their modal abundance, and the contribution of each mineral to the whole-rock REE budget remains to be quantified. Radiation damage (metamictization) caused by thorite and other U–Th-bearing minerals may facilitate the breakdown of these minerals and their neighbors during weathering, but this effect was not quantified.

4.1.3. μXRF Mapping

Micro-X-ray fluorescence mapping was used to characterize the distribution of REE and associated elements in the fresh granites at the centimeter scale (Figure 5). Because the analytical volume is equal to or larger than most REE-bearing grains (Section 3.2), the maps are interpreted in terms of element distribution only. Pixels with elevated Ce, La, Nd, and Y signals occur mainly along mineral boundaries and within alteration zones, consistent with the textural positions of the monazite, allanite, zircon, and apatite grains identified by SEM–EDS (Section 4.1.2). Y-rich pixels in B5-R may indicate xenotime, and Ti–Ca-rich pixels in B8-R were classified by AMICS as titanite; neither phase was confirmed by SEM–EDS, and both are therefore regarded as tentative. The AMICS area fractions of the accessory phases (≤0.03% of the mapped surfaces) are therefore not used as estimates of their abundance.

Sample B1-R shows Nd-rich domains (Figure 5a), and sample B5-R shows Y-rich domains near fine-grained minerals classified as tourmaline (Figure 5b). Th-rich pixels in B6-R2 coincide with biotite- and apatite-bearing domains (Figure 5c). Apparent Ce enrichment along alkali-feldspar boundaries in B7-R and in Ti-rich domains in B8-R (Figure 5d**,e**) may be partly caused by Ba $L\beta_1$ and Ti $K\beta$ interferences on Ce $L\alpha$ and is not interpreted further. Because boron is not detectable by μXRF, the AMICS "tourmaline" class is assigned from Fe–Mg–Al–Si signals alone and may include biotite or chlorite; the AMICS maps are therefore not used to infer mineral associations at the grain scale. Overall, the μXRF maps indicate that REE-bearing phases are concentrated along mineral boundaries and within alteration zones of the granites.

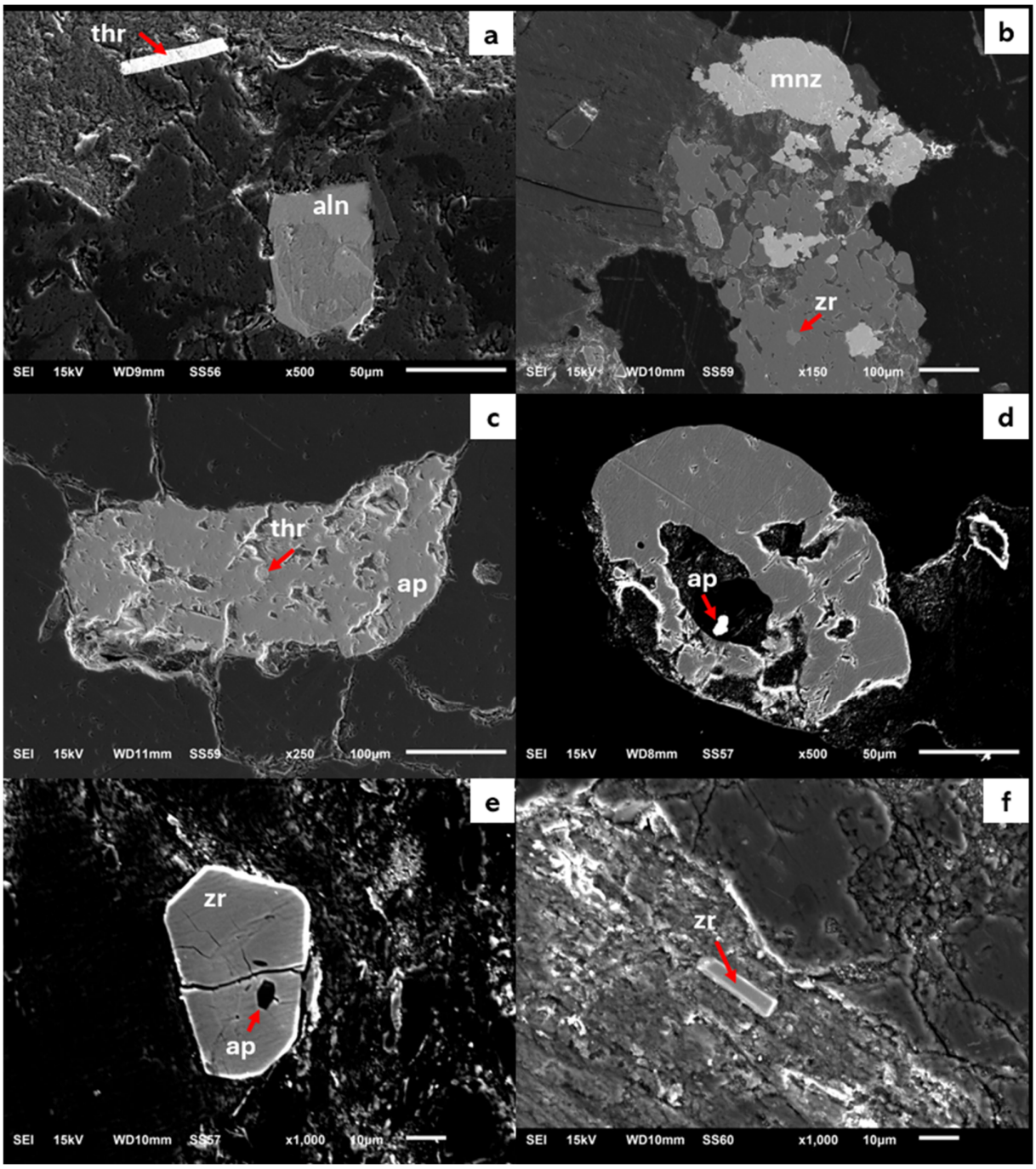


Figure 4. SEM images (secondary-electron mode) of REE- and Th-bearing accessory minerals. (**a**) B1-R: fine-grained (<50 µm) allanite-(Ce) and tabular thorite. (**b**) B5-R: irregular monazite and tiny zircon on feldspar surfaces. (**c**) B6-R1: thorite inclusions in coarse apatite with broken texture. (**d**,**e**) B6-R2 and B7-R: apatite inclusions (<20 µm) in euhedral zircon. (**f**) B8-R: tabular zircon on altered feldspar surfaces. Abbreviations: Aln = allanite-(Ce), Thr = thorite, Mnz = monazite, Zr = zircon, Ap = apatite.

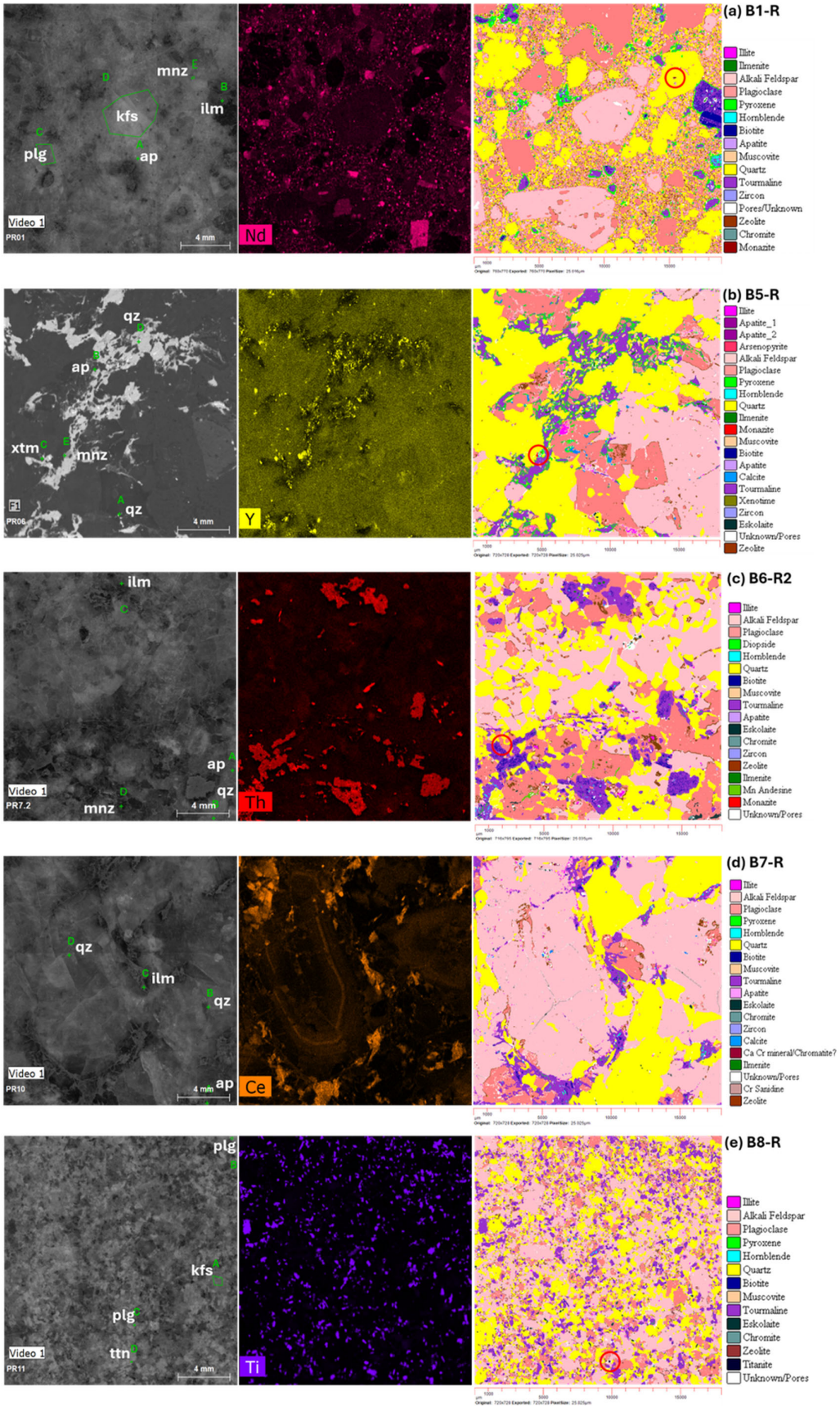


Figure 5. Polished granite surfaces (left), μXRF element-distribution maps (center), and AMICS phase-classification maps (right). (**a**) B1-R: neodymium (Nd, shown in pink) enrichment. (**b**) B5-R:

localized yttrium (Y) enrichment near minerals classified as tourmaline. (**c**) B6-R2: thorium (Th) enrichment in biotite- and apatite-bearing domains. (**d**) B7-R: apparent cerium (Ce) enrichment at alkali feldspar boundaries. (**e**) B8-R: apparent Ce enrichment in Ti-rich domains classified as titanite. The phase maps are indicative only, because accessory minerals smaller than the analytical volume yield mixed spectra and tourmaline cannot be verified without boron; grain-scale identification of REE-bearing minerals is based on SEM–EDS. Green letters in the left panels mark the μXRF point analyses, labeled with the identified mineral, and red circles in the phase maps highlight grains classified as accessory phases (e.g., monazite and titanite). The legends include phases assigned by the automated classification that are implausible in these granites (e.g., chromite, eskolaite, pyroxene, and zeolite), which reflect mixed-pixel misclassification. Abbreviations: Ilm = ilmenite, Bt = biotite, Ap = apatite, Xtm = xenotime, Mnz = monazite, Qz = quartz, Plg = plagioclase, Kfs = K-feldspar, Ttn = titanite.

4.1.4. X-Ray Diffractograms of Fresh Granite Rocks

Table 2 summarizes the detailed mineralogical compositions of the granite rock samples (R codes). Based on XRD diffractograms, the granite samples on Bangka Island (B1-R, B5-R, B6-R2, B7-R, and B8-R) have similar mineralogical compositions, consisting of quartz, K-feldspar, microcline, and albite. Semi-quantitative XRD analysis also indicates the presence of dickite in granite samples derived from biotite granite and hornblende–biotite granite, the dominant lithologies on Bangka Island [23]. Sample B6-R1, collected from the C horizon of profile B6, is a tourmalinized granite consisting of quartz (77.14%) and tourmaline (22.38%) without detectable feldspar; its composition (Table 3) reflects hydrothermal tourmalinization rather than weathering, and its high CIA value (85.6) therefore does not indicate weathering intensity.

Table 2. Semi-quantitative XRD mineralogical compositions of fresh granites (R codes) and weathered granites (S codes) from Bangka Island, showing the relative abundances across different weathering horizons.

No	Sample Code	Horizon	Mineral Content (%)												
			Qz	Kfs	Mc	Ab	Dck	Gbs	Kln	Chl	Ms	Nac	Sdl	Gth	Tur
1	B1-S1	O	74.25	n.d	1.61	n.d	n.d	5.62	17.06	1.40	n.d	n.d	n.d	n.d	n.d
2	B1-S2	A	49.11	n.d	n.d	n.d	n.d	7.41	39.81	n.d	n.d	n.d	n.d	n.d	n.d
3	B1-S3	B	58.03	n.d	n.d	n.d	n.d	11.06	n.d	n.d	7.90	23.01	n.d	n.d	n.d
4	B1-S4	B	32.50	n.d	53.55	n.d	n.d	4.52	n.d	1.78	7.61	n.d	n.d	n.d	n.d
5	B1-S5	B	75.00	n.d	1.80	n.d	n.d	20.00	1.30	1.90	n.d	n.d	n.d	n.d	n.d
6	B1-R	C	15.80	66.28	n.d	16.40	0.59	n.d	n.d	n.d	n.d	n.d	n.d	n.d	n.d
7	B2-S1	O	65.00	n.d	n.d	n.d	n.d	5.40	29.00	0.30	n.d	n.d	0.01	n.d	n.d
8	B2-S2	A	31.00	n.d	n.d	n.d	n.d	28.39	38.70	n.d	n.d	n.d	n.d	n.d	n.d
9	B2-S3	B	21.38	n.d	n.d	n.d	n.d	0.73	77.50	n.d	n.d	n.d	n.d	n.d	n.d
10	B3-S1	O	21.00	n.d	n.d	n.d	n.d	5.10	n.d	n.d	57.00	n.d	n.d	7.20	7.40
11	B3-S2	A	54.00	n.d	n.d	n.d	n.d	1.80	41.60	n.d	1.40	n.d	n.d	n.d	n.d
12	B3-S3	B	34.00	n.d	n.d	n.d	n.d	3.30	58.50	n.d	2.40	n.d	n.d	n.d	n.d
13	B3-S4	B	84.00	n.d	n.d	n.d	n.d	n.d	n.d	n.d	2.70	n.d	0.03	n.d	6.10
14	B4-S1	A	29.90	n.d	n.d	n.d	n.d	1.80	63.10	n.d	4.00	n.d	n.d	n.d	n.d
15	B4-S2	B	34.50	n.d	n.d	n.d	n.d	1.96	57.50	n.d	4.80	n.d	n.d	n.d	n.d
16	B5-S1	O	78.00	n.d	6.90	3.10	4.80	0.94	n.d	n.d	6.30	n.d	n.d	n.d	n.d
17	B5-S2	A	76.00	3.50	2.54	n.d	n.d	2.50	15.00	n.d	n.d	n.d	n.d	n.d	n.d
18	B5-S3	B	70.00	n.d	n.d	n.d	n.d	9.60	19.90	n.d	n.d	n.d	0.37	n.d	n.d
19	B5-S4	B	79.00	n.d	n.d	n.d	0.12	10.40	n.d	n.d	5.60	n.d	n.d	n.d	n.d
20	B5-S5	B	64.90	n.d	10.40	n.d	n.d	4.58	15.40	n.d	4.70	n.d	n.d	n.d	n.d
21	B5-S6	B	70.00	2.30	n.d	n.d	1.83	8.00	15.20	n.d	1.40	n.d	n.d	n.d	n.d

22	B5-S7	B	69.00	16.70	n.d	6.00	3.90	2.03	n.d	n.d	n.d	n.d	n.d	n.d	n.d
23	B5-S8	B	59.00	10.00	n.d	0.90	0.73	1.30	n.d	n.d	27.60	n.d	n.d	n.d	n.d
24	B5-R	C	53.10	n.d	15.53	30.06	0.13	n.d	n.d	n.d	n.d	n.d	n.d	n.d	n.d
25	B6-S1	O	81.00	11.60	n.d	3.10	n.d	0.92	n.d	n.d	2.90	n.d	n.d	n.d	n.d
26	B6-S2	A	37.30	11.80	n.d	n.d	n.d	3.50	22.80	n.d	9.70	n.d	n.d	n.d	15.00
27	B6-S3	B	60.00	0.50	n.d	n.d	n.d	n.d	28.60	n.d	9.00	n.d	0.21	n.d	1.50
28	B6-R1	C	77.14	n.d	n.d	n.d	n.d	n.d	n.d	n.d	n.d	n.d	0.48	n.d	22.38
29	B6-R2	C	33.60	n.d	37.50	24.00	3.96	n.d	n.d	n.d	n.d	n.d	n.d	n.d	n.d
30	B7-S1	O	63.42	n.d	6.80	n.d	n.d	2.23	27.55	n.d	n.d	n.d	n.d	n.d	n.d
31	B7-S2	A	63.62	n.d	4.80	n.d	n.d	1.96	29.41	n.d	n.d	n.d	n.d	n.d	n.d
32	B7-S3	B	78.18	n.d	n.d	n.d	n.d	0.60	21.05	n.d	n.d	n.d	0.17	n.d	n.d
33	B7-S4	B	46.14	n.d	19.01	n.d	2.15	10.94	n.d	21.76	n.d	n.d	n.d	n.d	n.d
34	B7-S5	B	41.61	n.d	34.10	n.d	3.82	12.05	n.d	8.42	n.d	n.d	n.d	n.d	n.d
35	B7-R	C	15.30	n.d	46.22	37.01	1.30	n.d	n.d	n.d	n.d	n.d	n.d	n.d	n.d
36	B8-S1	O	80.00	1.60	n.d	n.d	n.d	5.00	n.d	n.d	n.d	13.00	0.09	n.d	n.d
37	B8-S2	A	69.00	2.60	n.d	n.d	n.d	6.00	n.d	n.d	n.d	21.60	0.50	n.d	n.d
38	B8-S3	B	90.00	0.46	n.d	n.d	n.d	6.50	n.d	n.d	n.d	2.00	0.67	n.d	n.d
39	B8-R	C	26.78	46.08	n.d	24.89	2.25	n.d	n.d	n.d	n.d	n.d	n.d	n.d	n.d

n.d: not detected. Abbreviations: Qz = Quartz, Kfs = K-feldspar, Mc = Microcline, Ab = Albite, Dck = Dickite, Gbs = Gibbsite, Kln = Kaolinite, Chl = Chlorite, Ms = Muscovite, Nac = Nacrite, Sdl = Sodalite, Gth = Goethite, Tur = Tourmaline. Kln, Dck, and Nac were assigned by search–match of bulk-powder patterns and are referred to collectively as kaolin-group minerals in the text, because their polytypes and possible halloysite were not confirmed by specific methods (Section 4.2). Sdl (≤0.67%) is a search–match assignment that is mineralogically implausible in quartz-bearing granitic regolith and is not interpreted.

Table 3. Whole-rock geochemical data of major oxides, trace elements, and rare earth elements of the fresh and weathered granite samples, with the lithology of the fresh samples.

Sample Code	B1						B2			B3				B4	
	B1-S1	B1-S2	B1-S3	B1-S4	B1-S5	B1-R	B2-S1	B2-S2	B2-S3	B3-S1	B3-S2	B3-S3	B3-S4	B4-S1	B4-S2
Lithology	–	–	–	–	–	Bt granite	–	–	–	–	–	–	–	–	–
SiO_2 (wt.%)	60.70	50.20	56.90	65.10	57.20	71.40	59.98	39.93	57.49	38.41	63.65	69.23	70.11	64.34	65.42
TiO_2	0.40	0.54	0.38	0.23	0.48	0.23	0.67	0.52	0.68	0.81	0.11	0.10	0.11	0.13	0.08
Al_2O_3	33.60	41.00	37.50	26.80	34.70	13.70	20.98	30.21	25.55	26.62	23.82	21.62	19.82	23.49	23.28
P_2O_5	0.06	0.00	0.04	n.d	0.06	0.06	0.05	0.03	0.02	0.05	0.02	0.01	0.01	0.02	0.01
Fe_2O_3*	4.18	7.07	4.33	2.39	4.62	3.20	5.58	14.23	5.90	19.34	2.66	1.40	2.77	2.78	2.13
MnO	n.d	0.02	n.d	0.02	n.d	0.04	0.01	0.01	0.01	0.07	0.02	0.02	0.08	0.02	0.02
MgO	0.03	n.d	n.d	0.06	n.d	0.20	0.03	0.05	0.05	0.62	0.07	0.05	0.07	0.06	0.07
CaO	0.05	0.02	n.d	n.d	n.d	1.75	0.01	0.01	0.01	0.05	0.01	0.01	0.02	0.01	n.d
Na_2O	0.00	0.00	0.00	0.10	0.04	1.90	0.01	0.01	0.02	0.33	0.03	0.03	0.21	0.02	0.03
K_2O	0.77	0.66	0.51	5.00	2.25	7.19	0.03	0.07	0.31	2.52	0.44	0.55	0.39	0.37	0.39
CIA (%)	97.32	98.20	98.55	82.78	93.28	49.30	99.68	99.64	98.51	88.79	97.77	97.03	96.10	98.11	98.01
U	6.82	9.57	8.51	16.90	13.80	6.67	3.25	5.25	2.72	4.01	6.80	5.76	5.99	7.49	6.63
Th	61.40	78.40	73.90	73.30	68.60	32.50	32.80	69.60	40.40	40.70	48.40	49.30	40.30	82.80	54.80
La	6.00	11.30	9.40	15.10	9.70	51.60	4.70	3.70	2.50	18.30	6.20	10.10	6.10	5.80	5.80
Ce	57.60	203.00	278.00	107.00	194.00	104.00	5.90	5.80	5.80	31.90	18.20	27.10	20.10	13.60	15.20
Pr	1.19	2.33	1.93	3.61	1.99	11.60	0.78	0.62	0.33	3.50	1.67	3.17	2.06	1.68	1.81
Nd	4.20	7.40	6.40	11.80	6.60	39.90	2.60	2.10	1.10	11.00	5.60	11.20	7.90	6.10	6.50
Sm	1.10	1.60	1.20	2.70	1.50	8.00	0.60	0.40	0.30	2.00	1.20	2.50	2.10	1.70	1.80
Eu	0.10	0.20	0.10	0.30	0.20	0.90	0.10	n.d	n.d	0.50	n.d	n.d	n.d	n.d	0.09
Gd	0.80	1.30	1.20	2.30	1.50	7.50	0.50	0.50	0.30	1.70	1.10	2.20	1.60	1.90	1.20

Tb	0.11	0.17	0.18	0.28	0.17	1.10	0.06	0.06	n.d	0.25	0.19	0.40	0.26	0.35	0.20
Dy	1.10	1.10	1.10	1.70	0.90	6.80	0.40	0.50	0.30	1.50	1.60	2.60	1.80	2.80	1.60
Ho	0.20	0.20	0.20	0.40	0.20	1.40	n.d	n.d	n.d	0.30	0.40	0.60	0.40	0.80	0.40
Er	0.60	0.70	0.80	1.20	0.70	4.10	0.30	0.30	0.20	0.90	1.60	1.90	1.30	2.60	1.60
Tm	0.10	0.10	0.10	0.20	0.10	0.60	n.d	n.d	n.d	0.10	0.40	0.40	0.30	0.50	0.30
Yb	0.70	1.00	1.10	1.40	0.90	3.90	0.30	0.40	0.30	1.00	3.30	3.20	2.40	4.20	2.70
Lu	0.11	0.11	0.17	0.28	0.13	0.49	0.06	0.09	0.06	0.18	0.55	0.49	0.50	0.68	0.53
Y	4.00	5.40	6.10	9.00	5.10	38.20	2.10	2.20	1.40	6.10	10.90	15.80	10.50	22.60	9.80
Sc	4.00	6.00	6.00	5.00	5.00	4.00	8.00	11.00	10.00	25.00	7.00	5.00	7.00	5.00	4.00
LREY	70.99	227.13	298.23	142.81	215.49	223.50	15.18	13.12	10.33	68.90	33.97	56.27	39.86	30.78	32.40
HREY	6.92	8.78	9.75	14.46	8.20	56.59	3.22	3.55	2.26	10.33	18.94	25.39	17.46	34.53	17.13
TREY	77.91	235.91	307.98	157.27	223.69	280.09	18.40	16.67	12.59	79.23	52.91	81.66	57.32	65.31	49.53
LREY/HREY	10.26	25.87	30.59	9.88	26.28	3.95	4.71	3.70	4.57	6.67	1.79	2.22	2.28	0.89	1.89
Ce/Ce*	5.22	9.57	15.79	3.51	10.68	1.03	0.75	0.93	1.54	0.96	1.37	1.16	1.37	1.05	1.13
Eu/Eu*	0.32	0.42	0.25	0.37	0.41	0.35	0.56	0.61	0.91	0.83	0.24	0.12	0.15	0.15	0.19

Sample Code					**B5**								**B6**		
	B5-S1	**B5-S2**	**B5-S3**	**B5-S4**	**B5-S5**	**B5-S6**	**B5-S7**	**B5-S8**	**B5-R**	**B6-S1**	**B6-S2**	**B6-S3**	**B6-R1**	**B6-R2**
Lithology	–	–	–	–	–	–	–	–	Bt granite	–	–	–	Tourm. granite	Bt granite
SiO_2	71.22	72.62	66.74	72.83	71.94	72.86	74.49	73.70	74.03	79.19	66.82	64.46	74.76	73.71
TiO_2	0.23	0.24	0.24	0.23	0.21	0.21	0.16	0.20	0.41	0.29	0.34	0.43	0.24	0.24
Al_2O_3	14.30	16.82	21.28	16.70	17.43	16.84	14.26	15.13	11.94	10.69	17.98	21.57	11.56	13.23
P_2O_5	0.05	0.03	0.02	0.03	0.03	0.02	0.02	0.03	0.09	0.04	0.03	0.03	0.02	0.08
Fe_2O_3*	2.28	2.34	2.57	2.36	2.30	2.12	1.97	2.30	4.49	2.51	5.92	4.59	7.68	3.26
MnO	0.03	0.02	0.02	0.03	0.02	0.03	0.03	0.04	0.06	0.08	0.03	0.01	0.07	0.06
MgO	0.08	0.07	0.07	0.10	0.07	0.13	0.11	0.11	0.38	0.11	0.20	0.19	0.42	0.28
CaO	0.12	0.02	0.01	0.01	0.01	0.01	0.07	0.03	1.16	0.07	0.07	0.03	0.23	1.20
Na_2O	0.66	0.13	0.01	0.04	0.05	0.07	0.96	0.41	2.54	0.34	0.25	0.09	0.72	3.02
K_2O	2.74	1.39	0.48	0.87	1.28	1.92	4.95	4.58	4.92	2.86	1.49	1.29	0.31	4.81
CIA (%)	77.01	90.55	97.46	94.21	92.14	88.39	66.87	72.68	50.69	73.87	89.31	93.10	85.64	51.71
U	12.00	10.70	14.00	17.10	12.30	11.90	17.70	14.10	15.90	6.12	8.91	7.32	2.39	6.48
Th	70.80	79.30	97.90	81.60	82.80	80.20	74.40	74.90	64.50	38.10	42.10	35.90	13.70	35.50
La	53.40	46.30	43.90	50.90	43.60	48.00	64.30	50.40	112.00	56.10	82.00	151.00	13.40	54.60
Ce	151.00	151.00	165.00	187.00	188.00	234.00	187.00	183.00	226.00	138.00	148.00	158.00	26.40	112.00
Pr	14.30	12.70	12.20	13.50	11.60	12.10	15.50	13.20	25.00	12.30	16.20	31.00	2.99	13.30
Nd	49.60	42.90	40.70	47.70	41.30	44.30	55.60	46.20	85.50	43.50	56.20	108.00	10.60	48.70
Sm	10.40	8.80	8.20	9.50	8.70	8.70	11.70	10.20	14.70	7.90	9.90	19.70	2.00	9.50
Eu	0.10	<0.1	<0.1	0.10	0.10	0.10	0.20	0.20	0.50	0.50	1.20	2.70	0.20	0.80
Gd	8.30	6.50	6.90	8.00	6.90	7.30	9.90	7.60	12.90	6.70	8.40	16.90	1.60	9.20
Tb	1.08	0.87	0.92	1.06	0.95	0.92	1.50	1.07	1.85	0.77	1.14	2.39	0.20	1.28
Dy	6.20	4.60	5.10	5.20	4.60	4.20	8.40	6.20	9.80	3.80	5.70	11.70	1.00	6.60
Ho	1.20	0.80	1.00	1.00	0.90	0.90	1.60	1.10	1.80	0.60	1.00	1.90	0.20	1.10
Er	3.00	2.00	4.30	2.40	2.20	2.30	4.50	3.20	4.70	1.80	2.60	5.40	0.60	2.80
Tm	0.40	0.30	0.40	0.40	0.40	0.40	0.60	0.50	0.60	0.20	0.30	0.70	<0.1	0.40
Yb	3.10	2.10	2.60	2.70	2.60	2.50	4.40	3.00	3.60	1.80	2.40	4.80	0.60	2.40
Lu	0.44	0.37	0.46	0.44	0.41	0.39	0.63	0.56	0.52	0.24	0.31	0.70	0.11	0.35
Y	24.40	16.40	23.10	21.40	21.20	19.80	50.90	27.40	50.10	17.00	29.90	60.60	4.80	31.80
Sc	5.00	6.00	6.00	8.00	7.00	7.00	5.00	7.00	7.00	4.00	10.00	10.00	7.00	7.00
LREY	287.10	268.20	276.90	316.70	300.20	354.50	344.20	310.80	476.60	265.00	321.90	487.30	57.19	248.10
HREY	39.82	27.44	37.88	34.60	33.26	31.41	72.53	43.03	72.97	26.21	43.35	88.19	7.51	46.73
TREY	326.92	295.64	314.78	351.30	333.46	385.91	416.73	353.83	549.57	291.21	365.25	575.49	64.70	294.83
LREY/HREY	7.21	9.77	7.31	9.15	9.03	11.29	4.75	7.22	6.53	10.11	7.43	5.53	7.62	5.31
Ce/Ce*	1.32	1.51	1.72	1.73	2.02	2.35	1.43	1.72	1.03	1.27	0.98	0.56	1.01	1.01

Eu/Eu*	0.03	0.04	0.04	0.03	0.04	0.04	0.06	0.07	0.11	0.21	0.40	0.45	0.34	0.26
Sample Code	**B7**									**B8**				
	B7-S1	**B7-S2**	**B7-S3**	**B7-S4**	**B7-S5**	**B7-R**	**B8-S1**	**B8-S2**	**B8-S3**	**B8-R**				
Lithology	–	–	–	–	–	Bt granite	–	–	–	Hbl–Bt granite				
SiO_2	59.50	54.60	54.80	56.00	61.40	75.50	69.95	64.76	74.31	71.40				
TiO_2	0.49	0.53	0.51	0.39	0.33	0.20	0.44	0.50	0.32	0.28				
Al_2O_3	33.40	37.80	35.90	26.80	25.50	11.70	16.58	20.41	14.94	15.05				
P_2O_5	0.06	0.06	n.d	0.05	0.05	0.06	0.04	0.04	0.03	0.03				
Fe_2O_3*	5.66	6.13	8.24	10.10	4.62	3.19	2.95	3.84	3.39	2.88				
MnO	0.02	0.02	0.02	0.04	0.05	0.05	0.01	n.d	0.01	0.04				
MgO	n.d	n.d	n.d	0.15	0.20	0.22	0.05	0.06	0.03	0.41				
CaO	0.01	0.01	n.d	n.d	n.d	1.24	0.04	0.02	0.01	0.76				
Na_2O	0.00	0.00	0.00	0.11	0.32	1.62	0.05	0.03	0.01	1.83				
K_2O	0.50	0.41	0.20	5.91	7.17	6.04	0.66	0.50	0.20	6.03				
CIA (%)	98.35	98.79	99.40	80.29	75.47	50.52	95.02	97.02	98.35	57.95				
U	7.71	8.52	6.49	13.90	12.40	9.57	8.59	9.56	7.82	8.39				
Th	77.80	88.90	66.60	86.90	70.30	52.70	47.50	58.30	46.90	46.10				
La	12.60	15.30	16.00	16.00	31.90	46.10	14.30	18.10	11.60	29.20				
Ce	52.70	96.80	58.00	122.00	120.00	98.20	43.40	60.00	48.50	160.00				
Pr	2.53	3.05	2.90	3.52	6.64	10.10	2.64	3.52	2.56	6.99				
Nd	7.40	8.80	8.60	11.40	22.70	32.90	8.60	11.90	9.10	25.00				
Sm	1.30	1.90	1.50	2.10	4.20	6.40	1.70	2.30	1.80	4.70				
Eu	0.10	0.10	0.10	0.20	0.40	0.70	0.20	0.30	0.20	1.10				
Gd	1.00	1.20	1.30	2.00	3.30	5.50	1.40	1.90	1.50	3.80				
Tb	0.14	0.19	0.17	0.28	0.43	0.83	0.19	0.27	0.20	0.57				
Dy	0.80	1.10	1.00	1.70	2.60	5.30	1.20	1.60	1.20	3.10				
Ho	0.20	0.20	0.20	0.40	0.60	1.00	0.20	0.30	0.20	0.60				
Er	0.70	0.70	0.70	1.20	1.70	3.20	0.60	0.80	0.60	1.60				
Tm	0.10	0.10	0.10	0.20	0.20	0.40	n.d	0.30	0.10	0.30				
Yb	0.90	1.00	0.90	1.20	1.80	2.90	0.80	0.90	0.80	1.80				
Lu	0.14	0.14	0.13	0.23	0.27	0.37	0.12	0.13	0.12	0.32				
Y	4.40	6.00	6.00	10.00	15.50	29.40	5.10	7.10	5.30	15.90				
Sc	4.00	4.00	3.00	4.00	4.00	4.00	4.00	5.00	4.00	4.00				
LREY	77.63	127.15	88.40	157.22	189.14	199.90	72.24	98.02	75.26	230.79				
HREY	7.38	9.43	9.20	15.21	23.10	43.40	8.21	11.40	8.52	24.19				
TREY	85.01	136.58	97.60	172.43	212.24	243.30	80.45	109.42	83.78	254.98				
LREY/HREY	10.52	13.48	9.61	10.34	8.19	4.61	8.80	8.60	8.83	9.54				
Ce/Ce*	2.26	3.43	2.06	3.93	1.99	1.10	1.71	1.82	2.15	2.71				
Eu/Eu*	0.27	0.20	0.22	0.30	0.33	0.36	0.40	0.44	0.37	0.79				

Fe_2O_3* total iron oxides; Chemical Index of Alteration (CIA) determined by molecular proportions of $[Al_2O_3/(Al_2O_3 + CaO + Na_2O + K_2O)] \times 100$, where CaO is not from carbonate [40]; $Ce/Ce^* = Ce_N/(La_N \times Pr_N)^{1/2}$, $Eu/Eu^* = Eu_N/(Sm_N \times Gd_N)^{1/2}$ (where N is normalized by C1 chondrite). LREY = ΣLa–Gd; HREY = ΣTb–Lu + Y; TREY = LREY + HREY (Sc not included). Lithology: Bt = biotite, Hbl = hornblende, Tourm. = tourmalinized.

Figure 6a shows that sample B6-R2 contains the highest dickite content (~4%), followed by B8-R (2.25%), and B7-R (1.30%), whereas B1-R and B5-R contain less than 1%. The elevated dickite content in B6-R2 indicates that this sample underwent more extensive post-magmatic alteration than the other parent granites. Dickite does not, however, require high temperatures: in sedimentary basins, it forms by the transformation of kaolinite during burial diagenesis [48,49], and the thermochemical stability of dickite relative to

kaolinite is discussed by Fialips et al. [50]. The dickite in the studied granites may have formed by low-temperature hydrothermal alteration or by a comparable diagenetic transformation of earlier kaolinite, two origins that fluid-inclusion or stable-isotope data could distinguish; in either case, it records fluid–rock interaction at low to moderate temperatures that predates the present weathering. By contrast, the tourmalinized sample B6-R1 records boron-rich magmatic–hydrothermal fluids [51], so the parent rocks of profile B6 have a more complex alteration history than those of the other profiles. Although REE-bearing minerals were not detected, this may be because their contents were below the XRD detection limit [52].

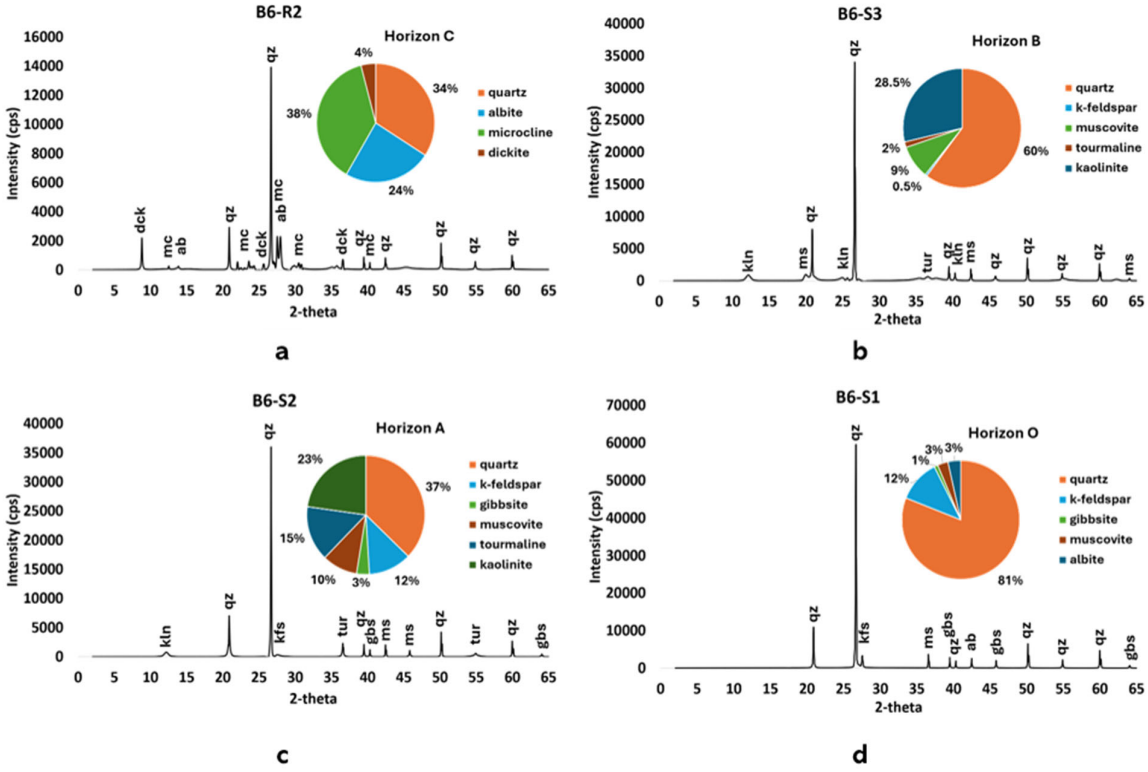


Figure 6. Mineralogical compositions from representatives: (**a**) granite sample of C horizon, and weathered granite profiles of (**b**) B horizon, (**c**) A horizon, and (**d**) O horizon. Abbreviations: Qz = Quartz, Kfs = K-feldspar, Mc = Microcline, Ab = Albite, Dck = Dickite, Gbs = Gibbsite, Kln = Kaolinite, Ms = Muscovite, Tur = Tourmaline.

4.2. Mineralogical Variations in Weathered Granite Profiles

The weathered samples (S codes) consist mainly of quartz, kaolin-group minerals, gibbsite, and micas, with relict feldspars in some lower B horizons (Table 2). The polytypes of the kaolin group (kaolinite, dickite, and nacrite) were assigned by search–match of bulk-powder diffractograms, which cannot separate them reliably without polytype-specific reflections or complementary methods [52], and 7 Å halloysite cannot be distinguished from kaolinite without an intercalation test [53]. These phases are therefore treated together as kaolin-group minerals, and the polytype assignments are regarded as provisional. Kaolin-group minerals reach 77.50% (B2-S3) and are most abundant in the lowland profiles B2–B4 (38.7–77.5% in their A and B horizons, except B3-S4). Gibbsite occurs in 31 of the 33 weathered samples (0.6–28.4%), with the highest contents in B2-S2 (28.39%) and B1-S5 (20.0%). In several lower B-horizon samples of the slope and foothill profiles (B1-S4, B1-S5, B5-S7, B5-S8, B7-S4, and B7-S5), gibbsite (1.3%–20.0%) occurs

together with relict K-feldspar or microcline (1.8%–53.6%) and little or no kaolinite (≤1.3%). Profile B8 contains no XRD-detectable kaolinite, but it contains a kaolin-group phase assigned to nacrite (2.0%–21.6%), together with gibbsite (5.0%–6.5%) and abundant quartz (69%–90%); its composition therefore does not indicate advanced lateritization, and its high CIA values (95.0–98.3) reflect the near-complete loss of alkalis and alkaline earths rather than a gibbsite-dominated (bauxitic) composition.

The other minerals are either inherited from the parent granites or formed near the surface. Dickite (0.12%–4.8%) occurs only in profiles B5 and B7, whose parent rocks also contain dickite, and is therefore inherited from the post-magmatic alteration of the granites (Section 4.1.4), as is chlorite after biotite, which reaches 21.8% in B7-S4. Muscovite, which cannot be distinguished from illite or sericite by bulk XRD, is locally abundant (27.6% in B5-S8 and 57% in B3-S1). Goethite occurs only in the O horizon of profile B3 (B3-S1, 7.2%), where it records the oxidation and accumulation of iron near the surface; goethite is an effective adsorbent [54], but this ferruginous horizon is not a gossan, because no sulfide mineralization is involved. Tourmaline, a weathering-resistant heavy mineral, occurs in profile B6 (1.5%–15%), where it is inherited from the tourmalinized granite B6-R1, and in profile B3 (6.1%–7.4%). Sodalite, which the search–match routine assigned at trace levels (≤0.67%), is implausible in quartz-bearing granitic regolith and is not interpreted. In the representative profile B6 (Figure 6), kaolinite is concentrated in the A and B horizons, at 22.8% and 28.6%, respectively (Figure 6b,c), whereas gibbsite is most abundant in the A and O horizons, at 3.5% and 0.9%, respectively (Figure 6c,d), and quartz persists in all horizons because it resists chemical weathering [30].

4.3. Geochemical Variations in Fresh Granites

The chemical compositions of five representative samples of granite (B1-R, B5-R, B6-R2, B7-R, and B8-R) are shown in Table 3. The high SiO_2 contents (71.40–75.50 wt.%) and low abundances of MnO (0.04–0.06 wt.%), MgO (0.20–0.41 wt.%), and CaO (0.76–1.75 wt.%) indicate an evolved felsic composition produced by advanced fractional crystallization. The systematic depletion of MgO and CaO relative to silica strongly suggests the progressive removal of early-crystallizing mafic minerals and plagioclase, a typical differentiation trend in granitic systems [55,56]. The relatively low TiO_2 (0.20–0.41 wt.%) further supports the fractionation of accessory minerals such as ilmenite or titanite, while the P_2O_5 contents (0.03–0.09 wt.%) are related to the occurrences of phosphate minerals such as apatite, monazite, and xenotime during the late stages of magmatic evolution [57]. Notably, the high K_2O contents (4.81–7.19 wt.%) and moderate Na_2O (1.62–3.02 wt.%) indicate enrichment in alkali feldspar and suggest an affinity with the high-K calc-alkaline series, typical of magmas derived from the melting of evolved continental crust [57,58].

The relatively high Al_2O_3 contents (11.70–15.05 wt.%) provide key constraints on alumina saturation and weathering intensity. On the total alkali–silica (TAS) diagram for plutonic rocks [59], all five samples plot in the granite field (as analyzed, SiO_2 = 71.40–75.50 wt.%; $Na_2O + K_2O$ = 7.46–9.09 wt.%; Table 4; Supplementary S3). Their molar ASI [$Al_2O_3/(CaO + Na_2O + K_2O)$] values of 0.97–1.07 and A/NK [$Al_2O_3/(Na_2O + K_2O)$] values of 1.26–1.30 classify B1-R as metaluminous and B5-R, B6-R2, and B7-R as weakly peraluminous [57], whereas B8-R has a higher ASI (1.38), probably raised by incipient alteration. Because the ASI is below the value of 1.1 commonly used to separate S-type granites [56] in four of the five samples, the regional S-type designation of the Klabat Granite (Section 2) is not evident from the ASI of these samples alone. On the QAP diagram [60,61], the visually estimated modal proportions of quartz, alkali feldspar, and plagioclase classify B1-R, B6-R2, and B7-R as biotite monzogranites, B5-R as a biotite syenogranite, and B8-R as a hornblende–biotite monzogranite; because the modal proportions are visual estimates, with standard deviations of 4–17 vol.% between fields of view (Supplementary S2),

these names are approximate, and B6-R2 lies close to the syenogranite–monzogranite boundary. The CIA values of the fresh granites (49.3–58.0) are typical of unweathered granitic rocks [40], with the slightly higher value of B8-R indicating incipient alteration. Sample B5-R exhibits distinctive geochemical features, with the highest Fe_2O_3 (4.49 wt.%) and TiO_2 (0.41 wt.%) contents among the biotite granites, suggesting enrichment linked to ilmenite. Conversely, B6-R2 has the highest Na_2O content, indicative of Na-rich albitization metasomatism, as evidenced by myrmekite texture [62]. Meanwhile, the B8-R sample has the highest Al_2O_3 content (15.05 wt.%), suggesting moderate alteration associated with weathering processes, which is consistent with its relatively high CIA value [40].

The five granite samples have total rare earth element (TREY) concentrations ranging from 243 to 550 ppm, with the lowest concentration in sample B7-R and the highest in sample B5-R. All samples are characterized by a pronounced enrichment of the light REE (LREY; La–Gd) relative to the heavy REE and Y (HREY; Tb–Lu + Y), as reflected by the dominance of Ce, La, and Nd, whereas the HREY is mainly represented by Y. Sample B5-R, which contains the highest P_2O_5 content (0.09 wt.%), also exhibits the highest TREY concentration, suggesting that the parent granite is enriched in REE-bearing phosphate minerals. In addition, all granite samples contain relatively high concentrations of Th (32.50–64.50 ppm) and U (6.48–15.90 ppm). Thorite, together with monazite and allanite, which commonly contain Th and U, accounts for these radioactive elements; such inclusions in biotite are surrounded by pleochroic halos [33,63].

Table 4. Chemical and modal classification of the fresh granite samples.

Sample	Mafic Minerals	TAS Field	ASI	A/NK	Alumina Saturation	QAP Field (Modal)	Rock Name
B1-R	Bt	Granite	0.97	1.26	Metaluminous	Monzogranite (3b)	Biotite monzogranite
B5-R	Bt	Granite	1.03	1.26	Weakly peraluminous	Syenogranite (3a)	Biotite syenogranite
B6-R2	Bt	Granite	1.07	1.30	Weakly peraluminous	Monzogranite (3b) §	Biotite monzogranite
B7-R	Bt	Granite	1.02	1.27	Weakly peraluminous	Monzogranite (3b)	Biotite monzogranite
B8-R	Hbl + Bt	Granite	1.38	1.58	Peraluminous ‡	Monzogranite (3b)	Hornblende–biotite monzogranite
B6-R1	Tur	n.a.	5.96	7.61	n.a.	n.a.	Tourmalinized granite

ASI = molar $Al_2O_3/(CaO + Na_2O + K_2O)$; A/NK = molar $Al_2O_3/(Na_2O + K_2O)$. TAS fields after [59]; QAP fields after [60] (3a, syenogranite; 3b, monzogranite), from visual modal estimates in six fields of view per thin section. ‡ Probably raised by incipient alteration (CIA = 58.0; 2.25% dickite). § Close to the syenogranite–monzogranite boundary ($100 \cdot P/(A + P) = 35.6$). n.a. = not applicable, because the composition of B6-R1 reflects hydrothermal replacement. Bt = biotite, Hbl = hornblende, Tur = tourmaline.

4.4. Geochemical Variations in Weathered Granite Profiles

The major oxide compositions of the studied samples vary significantly across the weathered profiles (Table 3). SiO_2 varies over a broad range, from 38.41 wt.% (B3-S1) up to 79.19 wt.% (B6-S1). Some weathered samples have lower SiO_2, such as B2-S2 (39.93 wt.%), B3-S1 (38.41 wt.%), and B2-S1 (59.98 wt.%), indicating silica loss during weathering processes. However, the weathered samples B6-S1 (79.19 wt.%) and B5-S7 (74.49 wt.%) contain relatively high SiO_2, possibly due to residual enrichment where silica accumulates relative to more mobile elements that have been removed.

Fe_2O_3 contents are enriched in the B2 and B3 profiles, reaching up to 19.34 wt.% (B3-S1). The B3-S1 sample indicates accumulation of iron oxides consistent with goethite

identified by XRD. Meanwhile, MgO and MnO remain consistently low in all samples; TiO_2 is also generally low but shows slight enrichment in weathered samples, with the highest values observed in B3-S1 (0.81 wt.%), B2-S3 (0.68 wt.%), and B2-S1 (0.67 wt.%). Furthermore, the low P_2O_5 (≤0.06 wt.%) implies that phosphorus becomes soluble or is largely lost to solution, with only limited retention in residual phases [64].

Na_2O, K_2O, and CaO, in contrast, are strongly depleted in the weathered granite samples. This depletion reflects weathering of plagioclase and K-feldspar, which transform into clay minerals during intense chemical weathering [65]. Concurrently, Al_2O_3 becomes relatively enriched in the weathered samples, reaching values of up to 41 wt.% (B1-S2) and approximately 37–38 wt.% in other samples (B1-S3 and B7-S2). These enrichments are consistent with the residual accumulation of aluminum-bearing minerals such as kaolinite and gibbsite and are associated with high CIA values (>98%) [18,30]. The CIA values in the weathered profiles (66.9–99.7) are generally above 70%, with the highest values observed in the O horizon (up to ~99%) and gradually decreasing with depth toward the C horizon. The high CIA values indicate extensive depletion of mobile cations (Ca^{2+}, Na^+, K^+), leaving behind immobile elements such as Al. The relationship between CIA and depth is consistent with previous studies describing the evolution of weathering profiles [40].

The TREY contents of the weathered samples span more than an order of magnitude, from 12.6 ppm (B2-S3) to 575.5 ppm (B6-S3), with a median of 157 ppm. The B1, B5, and B6 profiles show the highest TREY contents, reaching 308 ppm (B1-S3), 417 ppm (B5-S7), and 575.5 ppm (B6-S3), respectively, whereas the other profiles contain less than 215 ppm TREY. In Figure 7, the chondrite-normalized REE patterns show that the weathered samples are enriched in REE relative to chondrite [66]. The highest enrichment is observed in the B horizon of profile B6 (B6-S3), where the TREY content is 1.95 times that of the parent granite (B6-R2). TREY contents range from 18.4 to 326.9 ppm in the O horizon, from 16.7 to 365.3 ppm in the A horizon, and from 12.6 to 575.5 ppm in the B horizon.

Overall, most weathered granite samples show a pattern similar to the parent granites, with high LREY/HREY ratios. In addition, most samples show strong negative Eu anomalies ($Eu/Eu^* < 1$). Because the fresh granites display similarly negative Eu anomalies, this feature is interpreted as largely inherited from feldspar fractionation in the parent magmas rather than generated by weathering [67]. Moreover, B6-S3 is the only B-horizon sample with a pronounced negative Ce anomaly ($Ce/Ce^* = 0.56$); weak negative anomalies ($Ce/Ce^* = 0.75–0.98$) occur in some O- and A-horizon samples (B2-S1, B2-S2, B3-S1, and B6-S2), whereas the other weathered samples display positive Ce anomalies. Positive Ce anomalies ($Ce/Ce^* > 1$) commonly develop under oxidizing conditions, where Ce^{3+} is oxidized to the less soluble Ce^{4+} [6].

Based on chondrite-normalized REE patterns, profiles B1, B5, and B7 show consistent positive Ce anomalies that are absent in their fresh granites (Ce/Ce^* of 1.03–1.10 in the parent samples). Profile B8 also displays positive anomalies, although its parent granite already carries a pronounced positive anomaly ($Ce/Ce^* = 2.71$), so part of this signal is inherited. In contrast, profiles B2, B3, and B4—for which no C horizon is preserved, so their granitic parentage is inferred rather than directly observed—show comparatively low REE concentrations (depletion) and only weak Ce anomalies ($Ce/Ce^* = 0.75–1.54$). Compared with the other profiles, B6 shows the strongest REE enrichment, and its B horizon (B6-S3), which has a negative Ce anomaly, is interpreted as a zone of REE accumulation [68]; the form in which the REE are held in this horizon remains to be determined.

Because each panel of the REE diagrams shows the parent rock of the profile together with the range of the fresh granites, the REE patterns of the weathering horizons can be compared directly with those of their parent rocks: only the B horizon of profile B6 (B6-

S3) lies above the range of the fresh granites for all REE except Ce (Figure 7f), whereas the weathered horizons of the other profiles plot within or below this range for most REE.

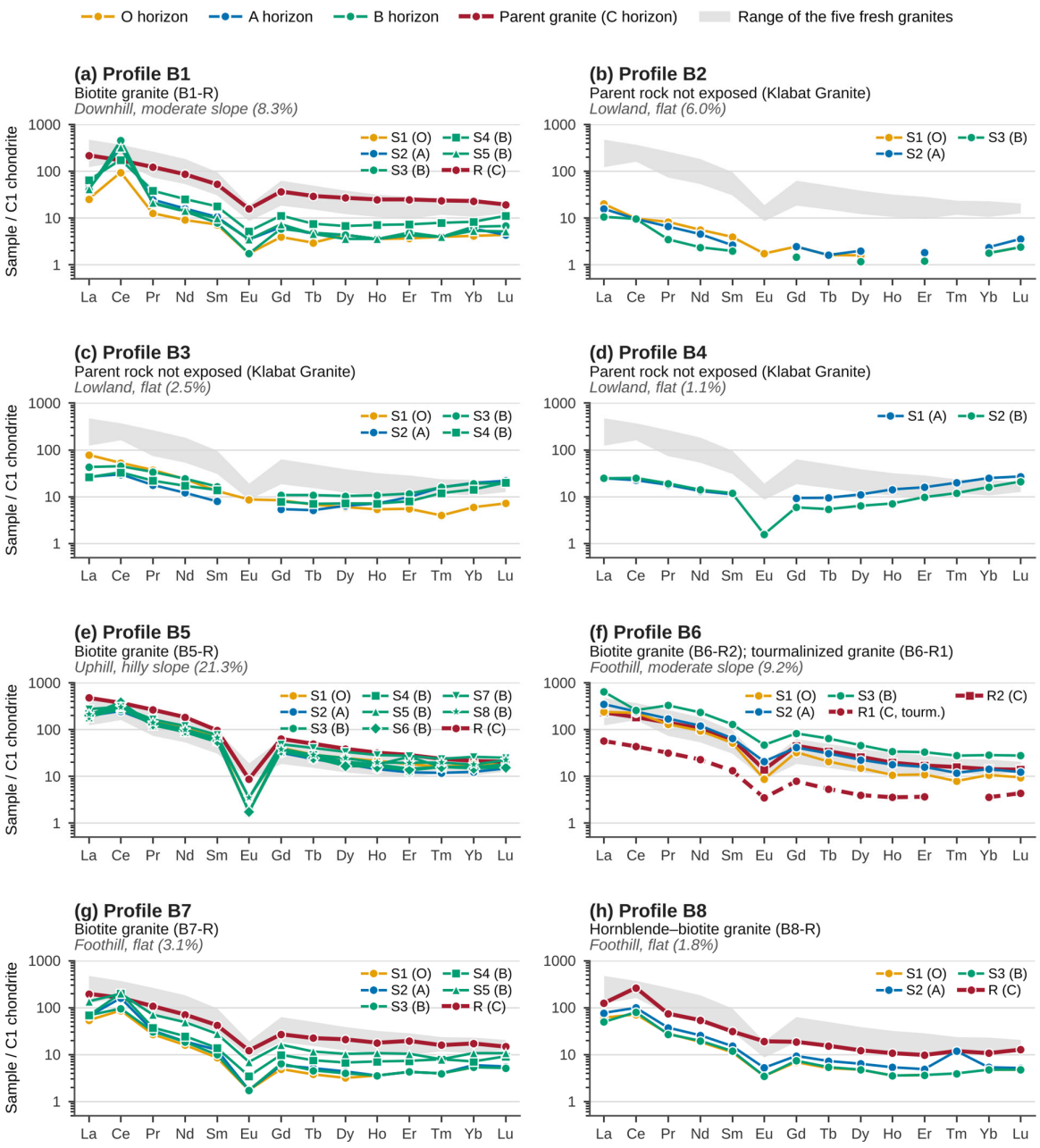


Figure 7. Chondrite-normalized REE patterns of the weathered granite profiles from Bangka Island: (**a**–**h**) profiles B1–B8 (normalization values from [66]). Each panel gives the parent rock of the profile and its topographic setting and slope gradient; the parent rocks of profiles B2–B4 are not exposed. Colors mark the weathering horizons (orange, O; blue, A; green, B; dark red, parent granite of the C horizon), and different symbols distinguish samples from the same horizon; the tourmalinized granite B6-R1 is shown by a dashed line. The grey field, repeated in every panel, shows the range of the five fresh granites (B1-R, B5-R, B6-R2, B7-R, and B8-R). Values below the detection limit are not plotted. Most profiles show LREE enrichment and a pronounced negative Eu anomaly.

5. Discussion

5.1. Vertical Evolution of Weathered Granite Profiles

The idealized vertical evolution of weathered granite profiles in the Bangka region typically consists of complete horizons (Figure 8). These horizons vary in color, texture, and mineral assemblages from the surface to bedrock, depending on weathering intensity. The upper O horizon is brownish and organic-rich, highly weathered, with elevated CIA values. Below it, horizon A is yellow and contains secondary minerals, particularly gibbsite and kaolinite. The B horizon is yellow-reddish and contains abundant kaolinite. Despite heavy alteration, the relict granitic textures are still visible to the naked eye in this horizon. At the bottom, the C horizon consists of relatively fresh granite rocks, with unaltered mineral textures; similar horizon sequences have been described in other tropical weathering profiles [18,32,33].

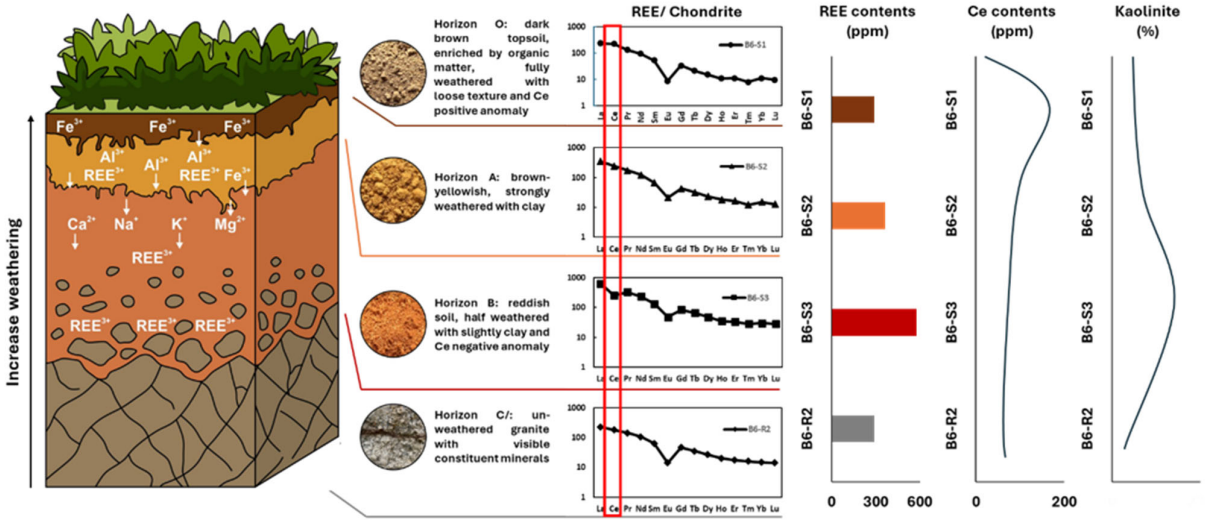


Figure 8. Schematic weathering columns illustrate REE redistribution along the representative weathering profile, Ce anomaly in chondrite-normalized patterns, Ce concentrations, and kaolinite accumulation; TREY is the sum of the lanthanides and Y. These features indicate potential REE enrichment within the weathered horizons. The red boxes mark Ce in the chondrite-normalized patterns.

On the basis of the SEM–EDS data, REE in the Bangka granites are hosted mainly by monazite-(Ce) and allanite-(Ce), with minor contributions from zircon and apatite, whereas thorite is the main Th-rich phase; xenotime and titanite are only tentatively identified (Table 5). REE-fluorocarbonate minerals were not detected; however, because phases with weak image contrast may be under-represented in the SEM observations, their absence cannot be confirmed, and such minerals have been reported from weathered granites in South Bangka [30]. During weathering, these minerals gradually break down and release REE into weathered profiles [64]. As weathering becomes more intense, REE are redistributed throughout the profiles, and the weathered horizons commonly show REE enrichment due to mineral dissolution, downward migration, adsorption onto clay minerals, and local precipitation of secondary REE minerals such as cerianite and rhabdophane [69].

Table 5. REE- and Th-bearing accessory minerals in the fresh granites, the techniques supporting their identification, and the resulting level of confidence. SEM–EDS is the primary evidence; petrography and μXRF are supporting evidence only.

Mineral	Samples	Petrography	SEM–EDS	μXRF/AMICS	Status
Monazite-(Ce)	B5-R	Inclusions in biotite (optical identification provisional)	P–Ce–La(–Pr) spectra	Ce–La–Nd-rich pixels	Confirmed
Allanite-(Ce)	B1-R	Brownish pleochroic grain in biotite	P-free Si–Ca–Fe–LREE spectrum	Not resolved	Confirmed
Thorite	B1-R, B6-R1	Not resolved	Th–Si spectra	Th-rich pixels (B6-R2)	Confirmed
Zircon	B5-R, B7-R, B8-R	Small inclusions (<50 μm)	Zr–Si spectra	Not used	Confirmed
Apatite	B7-R; B6-R1, B6-R2 (images)	Inclusions in biotite	Ca–P spectra (B7-R)	Not used	Confirmed (B7-R); tentative elsewhere
Xenotime	B1-R, B5-R, B6-R2	Small inclusions in biotite (optically uncertain)	Not confirmed	Y-rich pixels (B5-R)	Tentative
Titanite	B8-R	Not observed	Not observed	AMICS class (Ti–Ca pixels)	Tentative
REE fluorocarbonates	–	Not observed	Not detected *	Not resolved	Not detected *

Confirmed: identified by SEM–EDS spot analyses. Tentative: supported only by optical properties and/or μXRF element associations, which cannot resolve grains smaller than the analytical volume. * Phases with weak image contrast may be under-represented in the SEM observations, so their absence cannot be confirmed.

The geochemical and mineralogical data show that REE behavior changes vertically. In profile B6, the highest REE concentration (575.5 ppm TREY in B6-S3) coincides with a moderately high kaolinite content (28.6%) and a negative Ce anomaly (Ce/Ce* = 0.56), whereas the overlying O horizon has a positive Ce anomaly (Ce/Ce* = 1.27). This pattern is consistent with the oxidative retention of Ce^{4+} near the surface and the downward migration of the other, trivalent REE, which may be retained in the B horizon by adsorption onto clay minerals [16,32,70]. However, this co-occurrence does not demonstrate adsorption, which therefore remains a working hypothesis. Across the 33 weathered samples, TREY is not positively correlated with kaolinite (Spearman $\rho = -0.40$, $p = 0.02$) or with the kaolin-group minerals as a whole ($\rho = -0.36$, $p = 0.04$), nor with Fe_2O_3 ($\rho = -0.33$) or P_2O_5 ($\rho = 0.03$), but it decreases with increasing CIA ($\rho = -0.61$, $p < 0.001$); kaolinite abundance therefore does not control the bulk REE concentration of these profiles, and the most intensely weathered samples are depleted in REE. In addition, the P_2O_5 content of B6-S3 (0.03 wt.%) corresponds to a molar P/REY ratio of ~1.0, so that residual monazite and xenotime or secondary REE phosphates (e.g., rhabdophane) could host a substantial part of the REE, while cerianite may account for part of the Ce in the Ce-enriched upper horizons [69]. Fe oxyhydroxides cannot be excluded as REE hosts, although the negative correlation between TREY and Fe_2O_3 suggests that they are not the dominant control, and Mn oxides are probably minor given the low MnO contents (≤0.08 wt.%). The partitioning of REE among exchangeable, oxide-bound, and mineral-bound forms therefore remains unresolved; it should be determined by selective extraction, beginning with the ion-exchangeable fraction (e.g., 0.5 M $(NH_4)_2SO_4$ [9]), by separation and analysis of the clay fraction, and by in situ microanalysis.

In addition, kaolinite is another important weathering product. A strong association between kaolinite-rich horizons and REE enrichment has been reported in ion-adsorption

REE deposits in South China [7]. In this study, however, kaolinite abundance alone does not guarantee the formation of an ion adsorption REE deposit. Profiles B2, B3, and B4 illustrate this well: despite kaolinite contents of up to ~77%, their total REE concentrations remain below 100 ppm, and in profile B3 the kaolinite-free O-horizon sample (B3-S1) contains as much REE as the kaolinite-rich B-horizon sample (B3-S3). The limiting factor in these lowland profiles is therefore interpreted to be the REE supply from the parent material rather than the adsorption capacity of the clays, an interpretation that is consistent with the absence of a positive correlation between kaolinite and TREY in the whole dataset. Overall, the vertical evolution of these weathered profiles highlights the coupled effects of mineral transformation and geochemical processes in controlling REE redistribution and the development of potential enrichment zones within tropical granitic regoliths [71,72].

5.2. Controls on REE Mobility and Enrichment

As discussed above, REE preservation in Bangka Island is influenced by mineralogical parent granites, element mobility under redox conditions, and weathering intensity. Although Bangka Island is located in the tropical region of Southeast Asia and experiences extreme denudation rates exceeding 1000 t/km^2/year [33], the sampling locations have been intensively weathered under wet and dry seasons, with average temperatures of 27 °C and approximately 2000 mm of annual rainfall [29,30]. While these conditions readily mobilize REE and promote the formation of ion-adsorption REE deposits, the actual preservation of REE within the weathering profiles is highly controlled by geomorphological landscape and local climatic conditions [18,69,73–75].

A further consideration is the composition of the parent granite, whose phosphate minerals monazite and xenotime are fairly resistant to chemical weathering [76]. However, the pleochroic halos in biotite show that U- and Th-bearing accessory minerals are present; radiation damage in these minerals may facilitate their breakdown and the release of REE during weathering [33]. The μXRF elemental maps display relatively high Th concentrations in the B6 parent granite compared with the other granite samples. The idealized B6 weathering profile shows a B horizon whose TREY content is about twice that of the parent granite. Although this horizon shows depleted P_2O_5 contents, this depletion, together with the radioactive accessory minerals observed in the granites, is consistent with metamictization-assisted breakdown of REE-bearing phosphates, which would then act as the primary source of REE in the weathering profile [33].

As illustrated in Figure 9, topography appears to strongly influence REE mobility and enrichment in the weathered granite profiles by regulating erosion rates and slope stability, working in concert with the mineralogical and geochemical controls described above. The B5 profile, located on hilly slopes, is strongly affected by erosion and intensive mechanical weathering processes, despite the parent granite at this location containing relatively high REE concentrations. In contrast, the B1 and B6 profiles developed on moderate slopes, which provide more stable conditions for forming thick weathering horizons, especially the B horizon. The B6 profile shows the strongest REE enrichment, probably because the low erosion rate on moderate slopes allows the REE released in the upper horizons to accumulate in the B horizon [16,77], where they may be retained by clay minerals or by secondary phases, in line with the mid-slope REE accumulation maxima reported from ion adsorption profiles in South China [20]. The two moderate-slope profiles nevertheless behave differently—B6 is strongly enriched whereas B1 is not—showing that a favorable slope is necessary but not sufficient, and that parent-rock fertility and horizon mineralogy exert equally strong control.

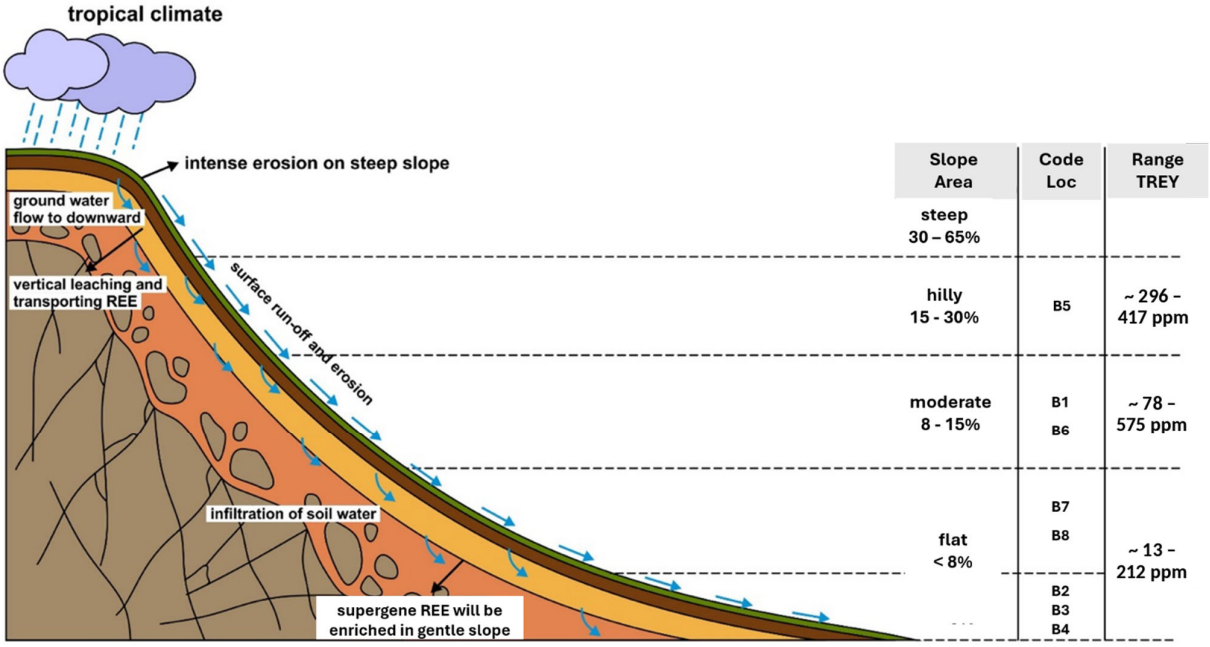


Figure 9. Conceptual model linking slope gradient, weathering processes, and total REE concentrations across the weathered granite profiles. It shows that moderate-slope areas provide the most favorable setting for REE enrichment. The TREY ranges are those of the weathered samples in each slope class (sum of the lanthanides and Y, without Sc).

Conversely, the weathered profiles located at the foothills and lowlands with flat slopes (B2, B3, B4, B7, and B8 profiles) tend to show limited REE enrichment. In these low-relief settings, the limiting factor is not mechanical stripping but prolonged water saturation: lateral groundwater flow promotes leaching and dispersal of the released REE, and much of the surrounding weathered material has been reworked into the alluvial deposits of the valleys and coastal plains rather than being retained for in situ adsorption [78]. The B1 profile, in contrast, although located on a moderate slope, shows no REE enrichment in its B horizon (B1-S3), which contains gibbsite and a kaolin-group phase assigned to nacrite (Section 4.2) but no XRD-detectable kaolinite; gibbsite is a less effective adsorbent of REE ions than kaolinite. The kaolinite-rich A horizon of the same profile (B1-S2, up to ~39.8% kaolinite) displays positive Ce anomalies (Figure 7a), indicating that it acts as a REE leaching zone; clay abundance alone therefore does not ensure REE retention.

The lithology of the parent rocks (Table 4) is a further potential control. The four biotite granites (B1-R, B5-R, B6-R2, and B7-R) have similar mineral assemblages, and three of them have similar TREY contents (243–295 ppm), yet the B horizons of their profiles range from depleted to enriched relative to the parent rock (enrichment factors, i.e., maximum B-horizon TREY divided by parent TREY, of 0.76–1.95). Parent-rock lithology alone therefore cannot explain the contrasting enrichment among these profiles, which is more consistent with the topographic and mineralogical controls discussed above. The most REE-rich granite (B5-R, 550 ppm TREY, with the highest P_2O_5 content) does not produce the most enriched profile, which we attribute to erosion on its hilly slope. The only hornblende-bearing granite (B8-R) has a pronounced positive Ce anomaly (Ce/Ce* = 2.71) that is inherited by its weathered horizons, and its profile is the least enriched (enrichment factor 0.33), but the effect of lithology cannot be separated from that of its flat foothill setting. Finally, the tourmalinized granite B6-R1 contains much less TREY (65 ppm) than the biotite granite B6-R2 (295 ppm), suggesting that hydrothermal tourmalinization locally depleted the REE; the REE accumulated in the B horizon of profile B6 were therefore

most likely derived from the biotite granite. A rigorous assessment of lithological control would require profiles developed on each granite type under the same geomorphological conditions.

Several limitations of this study warrant acknowledgment. The eight profiles are distributed across Bangka Island rather than along a single hillslope sequence, so site-specific factors—residual differences in parent-granite composition, exposure history, and local microclimate—cannot be fully separated from the influence of slope, and the geomorphological interpretation presented here should therefore be regarded as indicative rather than definitive. The shared parent lithology of the Late Triassic Bangka granitoids, the uniform tropical climate, and the convergence of independent mineralogical and geochemical indicators nevertheless lend support to the observed relationship between slope class and REE enrichment. Testing this relationship through systematic sampling of complete slope sequences developed on a single granite body, ideally combined with constraints on denudation rates and regolith ages, is an important direction for future work.

5.3. Grade, Thickness, and Exploration Significance

The REE grades of the studied profiles are low. The highest TREY content (575.5 ppm in B6-S3) corresponds to ~0.07 wt.% total rare earth oxides (TREO, including Y_2O_3). Only two of the 33 weathered samples (B6-S3 and B5-S7) reach 0.05 wt.% TREO, and 23 samples contain less than 300 ppm TREY. The REE distribution is LREE-dominated: La, Ce, and Nd account for 72% of the TREY in B6-S3 (median 81% in the weathered samples), and HREY (Tb–Lu + Y) represent only 3%–17% of the TREY in the samples with more than 200 ppm TREY. Although Nd and Pr, which make up 24% of the TREY in B6-S3, are in demand for advanced technologies [1], the low HREY proportion limits the value of these profiles. Most importantly, the ion-exchangeable REE fraction, which is the fraction recovered by salt leaching in ion-adsorption deposits [4,5], was not determined. Whole-rock concentrations obtained after four-acid digestion include REE held in residual minerals; they therefore represent total rather than recoverable grades, and a comparison with industrial cut-off grades requires ion-exchangeable REE data.

In profile B6, the REE-enriched B horizon (sample B6-S3) extends from 1.6 to 3.8 m depth, an exposed thickness of 2.2 m, and is overlain by 1.6 m of O and A horizons containing 291–365 ppm TREY. In profiles B1 and B5, the B horizons are 2.0 and 3.8 m thick but contain 157–308 ppm and 315–417 ppm TREY, respectively, i.e., no more than 1.1 times the TREY of their parent granites. These thicknesses were measured on single natural or excavated exposures and represent only the exposed part of the regolith; the lateral continuity of the enriched horizon, the depth to fresh bedrock away from the exposures, and the thickness of barren overburden are unknown. Resource tonnage, stripping ratio, and mineability will therefore require drill-hole data, and the present results provide a basis for targeting rather than for industrial evaluation.

For these reasons, the indicators derived in this study are presented as descriptive characteristics of the most enriched profile relative to the other profiles (Table 6) rather than as quantitative exploration thresholds. Slope position, profile completeness, parent-rock TREY, and B-horizon mineralogy are necessary but not sufficient conditions—profile B1 shares the geomorphological characteristics of B6 but is not enriched, and the lowland profiles contain abundant kaolinite but little REE—whereas the enrichment factor of the B horizon relative to the parent granite and the Ce anomaly distinguish B6 from all other profiles. Because only one of the eight profiles is strongly enriched, quantitative thresholds are best defined at a later stage, using ion-exchangeable REE data and grade–thickness data from systematic pitting or auger drilling across the moderate-slope settings. The profiles are therefore regarded as REE-enriched regolith that warrants further

investigation, beginning with the determination of ion-exchangeable REE in the B horizons, rather than as an ion-adsorption REE resource.

Table 6. Characteristics of the most enriched profile (B6) compared with the other profiles.

Characteristic	B6 (Most Enriched)	Other Profiles	Remark
Slope gradient	9.17% (moderate)	B1 8.3%; B5 21.3%; B2–B4, B7, B8 1.1%–6.0%	Shared with B1, which is not enriched
Relative elevation	18.6% of local peak (foothill)	B1 27.6%; B5 53.3%; B7, B8 10.8%–11.8%	Same class as B7 and B8, which are not enriched
Profile completeness and B-horizon thickness	Complete O–A–B–C profile; B horizon 2.2 m (exposed)	B horizons 1.2–3.8 m; no C horizon in B2–B4	Lateral continuity unknown
Parent-rock TREY	295 ppm (B6-R2)	243–550 ppm	Not discriminating within Bangka
B-horizon mineralogy and weathering	Kaolinite 28.6%; CIA 93.1	B1 kaolinite ≤ 1.3% (gibbsite and nacrite instead); B5, B7 ≤ 21.1%; B2–B4 up to 77.5% but TREY ≤ 82 ppm	Not sufficient on its own
Enrichment factor (maximum B-horizon TREY/parent TREY)	1.95	B1 1.10; B5 0.76; B7 0.87; B8 0.33	Distinguishes B6
Ce anomaly (Ce/Ce*)	0.56 in the B horizon beneath 1.27 in the O horizon	B horizons 1.13–15.79	Distinguishes B6
Whole-rock grade	0.069 wt.% TREO	≤0.050 wt.% TREO (maximum B5-S7)	Low; recoverable fraction unknown
Ion-exchangeable REE	Not measured	Not measured	Required for economic evaluation

TREY excludes Sc; TREO includes Y_2O_3. Enrichment factor = maximum TREY of the B horizon divided by the TREY of the parent granite. The characteristics are descriptive and are not exploration thresholds; they are derived from eight profiles of which only B6 is strongly enriched.

5.4. Comparison with Other Weathered Granite Profiles

Weathered granites of the Southeast Asian Tin Belt provide the most direct comparison for the Bangka profiles. In the Toboali area of South Bangka, the weathered crust is developed on an S-type biotite granite whose total REE contents (1081–1279 ppm) are much higher than those of the granites studied here (243–550 ppm TREY); the main REE-bearing minerals of that granite are REE fluorocarbonates (synchysite and parisite), accompanied by REE phosphates and silicates, and monazite, xenotime, and zircon persist as residual minerals in the weathered profiles [30]. One of the Toboali profiles is strongly depleted in REE where weathering intensity is high and gibbsite is present, whereas the other shows Ce enrichment in its lower part, attributed to cerianite and/or Fe–Mn (hydr)oxides [30]. These observations parallel those at Bangka, where the most intensely weathered samples are depleted in REE (Section 5.1), and they indicate that the REE content of weathered tin-belt granites depends strongly on the REE mineralogy of the parent rock and on weathering intensity. REE behavior during weathering has also been documented for ion-adsorption-type mineralization and phosphate-bearing granites in Thailand [12,69] and for deeply weathered, geochemically contrasting and metamictized granites in Peninsular Malaysia [32,33]. Because monazite-(Ce), which is resistant to chemical weathering [76], and allanite-(Ce) are the confirmed REE hosts at Bangka and REE fluorocarbonates were not detected, a substantial part of the REE budget probably remains in residual phases, which may explain why the weathered horizons of most Bangka profiles contain no more than ~1.1 times the TREY of their parent granites. Weathered tin-belt

granites with a similar accessory mineralogy are therefore expected to show REE concentrations of the same order as at Bangka, whereas stronger enrichment would require a larger proportion of the REE in weathering-susceptible minerals. This comparison is limited by the small number of documented profiles and by differences in sampling and analytical methods among the studies.

5.5. Clay Minerals, REE and Heavy Minerals, and Genetically Related Deposits

The clay minerals record both the hypogene history of the parent granites and the supergene processes of the present weathering cycle (Section 4.2). Dickite in the fresh granites (0.13%–3.96%) and in profiles B5 and B7, together with chlorite after biotite and sericitic muscovite, is inherited from post-magmatic alteration (Section 4.1.4), whereas kaolinite, gibbsite, and goethite are supergene. The supergene assemblage changes with the landscape position. In the lower B horizons of the slope and foothill profiles B1, B5, and B7, gibbsite occurs with relict feldspar and little or no kaolinite, which suggests that feldspar altered directly to gibbsite where the saprolite is freely drained and silica is rapidly removed. In contrast, the lowland profiles B2–B4 are dominated by kaolin-group minerals (38.7%–77.5% in their A and B horizons, except B3-S4), consistent with the retention of silica in less well-drained lowland regolith, and the B horizon of the moderately sloping profile B6 contains kaolinite (28.6%) without gibbsite. Because kaolinite and halloysite, which were not distinguished here, differ in their capacity to adsorb REE [16], and because TREY is not positively related to the kaolin-group content of our samples (Section 5.1), the clay mineralogy is regarded mainly as a record of weathering and drainage conditions rather than as a direct measure of REE enrichment. At the same time, the kaolin-rich lowland regolith represents a potential industrial-mineral (kaolin) resource that belongs to the same weathering system.

The heavy minerals behave differently from the clay minerals. In the profiles with exposed parent rocks, Th is retained or enriched in all weathered horizons (1.0–2.4 times the parent granite), as is TiO_2 in profiles B1, B6, B7, and B8 (1.0–2.7 times), whereas TREY is mostly lower than in the parent granite (0.28–1.10 times), except in profile B6 (0.99–1.95 times). The resulting increase in the Th/TREY ratio, to 1.5–6.8 times that of the parent in profiles B1, B5, B7, and B8 but only 0.5–1.1 times in B6, indicates that weathering-resistant Th- and Ti-bearing heavy minerals (e.g., monazite, thorite, zircon, ilmenite, and other Ti oxides) accumulated residually, whereas a large part of the REE released from less resistant hosts was lost from these profiles; only profile B6 retained the released REE. Among the REE minerals identified in the parent granites, allanite-(Ce) and apatite are readily decomposed during weathering [4,7], so that the REE they contain can be released into the regolith, whereas monazite-(Ce) and, where present, xenotime resist weathering [30,76] and, together with zircon, remain as residual grains that can be transferred to placers. The released REE are retained in the regolith only where they are adsorbed or fixed in secondary phases, such as rhabdophane-type phosphates or cerianite, which are inferred from the geochemical data but were not observed (Section 5.1). Tourmaline, another resistant heavy mineral, is inherited from the tourmalinized granite in profile B6 (15% in B6-S2) and also occurs in the lowland profile B3 (6.1%–7.4%). From a sedimentary point of view, the lowland profiles differ from the slope profiles. B2 has TiO_2 contents (0.52–0.68 wt.%) above those of all fresh granites (0.20–0.41 wt.%), and the O horizon of B3 (B3-S1) combines the highest TiO_2 content (0.81 wt.%) with abundant muscovite (57%), tourmaline, and goethite. These compositions, together with the flat REE patterns of the A and B horizons of profiles B3 and B4 ($(La/Yb)_N$ = 0.9–2.1; Figure 7c,d), suggest that the lowland regolith includes transported (colluvial–alluvial) material, possibly derived in part from the metamorphic rocks of the Pemali Complex near B3, in which heavy minerals were concentrated by hydraulic sorting rather than by in situ weathering alone. Grain-

size separation and heavy-mineral analysis of these horizons would be required to test this interpretation.

These mineral associations link the regolith-hosted REE enrichment to the other deposit types of the Bangka tin province (Table 7; Figure 10). In the headwater zone, the granites host primary cassiterite mineralization in greisen and vein systems [15,23], and the tourmalinization (B6-R1) and dickite-bearing alteration of the parent rocks (Section 4.1.4) record post-magmatic fluid activity. Chemical weathering of the granites produced the kaolin-rich saprolite and the REE-enriched B horizons described here, while resistant heavy minerals, such as cassiterite, monazite, xenotime, zircon, and ilmenite, were concentrated residually in the regolith and then, by mass wasting and fluvial transport, in colluvial and alluvial placers [24,25,28,38]. During the Quaternary, sea-level fluctuations repeatedly exposed and flooded the Sunda Shelf [79], so that fluvial placers were reworked into coastal and offshore placers, which on Bangka also contain monazite and xenotime [15,27]. Primary tin mineralization, kaolin- and REE-bearing regolith, and placers are therefore successive products of one granite-derived mineral system, separated in space by the landforms and land-forming processes of the island. Similar mineralogical–geomorphological linkages have been used as exploration tools for REE deposits elsewhere [80]. For exploration, the REE-bearing heavy minerals of the placers (mainly monazite and xenotime, in which the REE are fixed in resistant phosphates) and the REE released into the regolith are complementary rather than competing targets: granites whose REE reside mainly in resistant phosphates feed placers, whereas the ion-adsorption potential of the regolith depends on the proportion of REE held in weatherable minerals (Section 5.4).

Table 7. Deposit types of the granite-derived mineral system on Bangka Island, their landscape position, and their characteristic clay and heavy minerals.

No.	Deposit Type	Landscape Position (Hydrographic Zone [41])	Main Processes	Characteristic Minerals	REE Carriers	Evidence (This Study) and References
1	Primary Sn in greisen and veins; tourmalinization	Granite hills (headwater zone)	Magmatic–hydrothermal; later low-temperature alteration	Cassiterite, tourmaline, muscovite; dickite	Monazite, allanite, xenotime, zircon (accessory)	Tourmalinized granite B6-R1; dickite in the fresh granites; [15,23]
2	Kaolin-rich regolith	Lower slopes and lowlands (track and deposition zones)	Chemical weathering of feldspar; retention of silica	Kaolin-group minerals (≤77.5%), gibbsite	Possibly adsorbed REE (not demonstrated)	Profiles B2–B4 and B6 (Table 2)
3	Regolith-hosted REE (B horizon)	Moderate lower slopes (track zone)	Release of REE, oxidation of Ce near the surface, downward accumulation of REE^{3+}	Kaolinite, Fe oxyhydroxides, secondary phosphates	Adsorbed REE, rhabdophane-type phosphates, cerianite (inferred)	B6-S3 (575.5 ppm TREY); [29,30,69]
4	Residual heavy minerals in regolith	Hillslopes (track zone)	Residual enrichment of resistant minerals	Monazite, thorite, zircon, ilmenite, tourmaline	Monazite, zircon	Th up to 2.4 and TiO_2 up to 2.7 times the parent (Table 3)
5	Colluvial–alluvial placers	Foothills, valleys, and lowlands (deposition zone)	Mass wasting, fluvial transport, and hydraulic sorting	Cassiterite, monazite, xenotime, zircon, ilmenite, tourmaline	Monazite, xenotime, zircon	Ti-, mica-, and tourmaline-rich lowland horizons (B2, B3); [24,25,28,38]

6	Coastal and offshore placers	Coast and Sunda Shelf (deposition zone)	Marine reworking during Quaternary sea-level changes	Cassiterite, monazite, xenotime, zircon, ilmenite	Monazite, xenotime	[15,27,79]

Deposit types 1, 5, and 6 are known from the literature cited; types 2–4 are documented in this study. Inferred REE hosts in type 3 are discussed in Section 5.1.

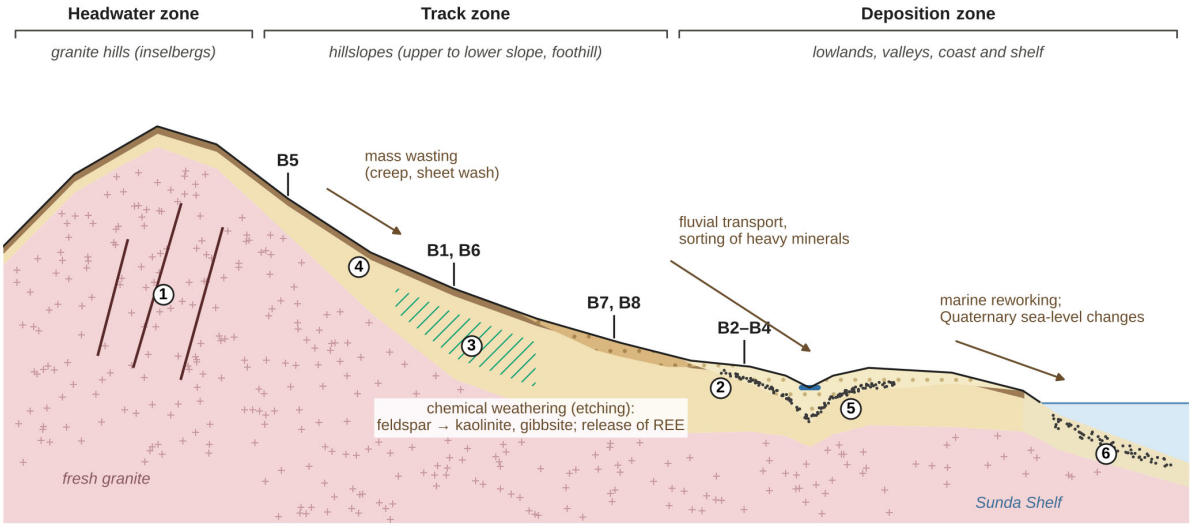


Figure 10. Schematic cross-section (not to scale) of the granite-derived mineral system on Bangka Island, showing the hydrographic zones [41], the main land-forming processes, the related deposit types (numbers as in Table 7: 1, primary Sn in greisen and veins and tourmalinization; 2, kaolin-rich regolith; 3, regolith-hosted REE (B horizon); 4, residual heavy minerals in the regolith; 5, colluvial–alluvial placers; 6, coastal and offshore placers), and the landscape positions of the studied profiles (B1–B8).

5.6. Terrain Analysis and Land-Forming Processes

In terms of the landscape maturity classes of Dill et al. [41], Bangka can be tentatively regarded as a super-mature landscape: a low-lying, deeply weathered plain with isolated granite hills rising to 705 m (Section 2), in which pervasive chemical weathering has produced residual kaolin- and REE-bearing regolith and in which the products of erosion are stored as placers. Within this landscape, the studied profiles occupy different positions along the hydrographic continuum from the headwater zone to the deposition zone [41] (Table 8). Profile B5 lies on the hilly upper slope of a low hill (at 53.3% of the height of the local peak; 21.3% slope gradient), in the erosional part of the track zone; profiles B1 and B6 lie on moderate lower slopes (8.3%–9.2%; at 18.6%–27.6% of the local peak height), where complete profiles are preserved; B7 and B8 lie on flat foothills (1.8%–3.1%), and B2–B4 on flat lowlands (1.1%–6.0%) in the deposition zone.

Table 8. Terrain parameters, hillslope elements, hydrographic zones, and maximum B-horizon TREY of the profiles.

Profile	Altitude (m a.s.l.)	Slope Gradient (%)/Angle (°)	Relative Elevation (%)	Hillslope Element	Hydrographic Zone [41]	Max. B-Horizon TREY (ppm)/EF
B1	80	8.3/4.7	27.6	Lower backslope	Track	308/1.10
B2	18	6.0/3.4	–	Lowland plain	Deposition	12.6/–
B3	49	2.5/1.4	–	Lowland plain	Deposition	81.7/–

B4	35	1.1/0.6	–	Lowland plain	Deposition	49.5/–
B5	64	21.3/12.0	53.3	Upper backslope	Track (erosional)	417/0.76
B6	91	9.17/5.2	18.6	Lower backslope	Track	575.5/1.95
B7	70	3.1/1.8	10.8	Footslope	Track–deposition transition	212/0.87
B8	15	1.8/1.0	11.8	Footslope	Track–deposition transition	83.8/0.33

Altitude, slope gradient, and relative elevation from Table 1; slope angle = arctangent of the gradient. Hydrographic zones were assigned from the landscape position of each profile and checked against the DEM-derived parameters in Table 9 (Section 3.4). EF = maximum B-horizon TREY divided by the TREY of the parent granite.

The numerical classification of the profiles by slope angle and altitude [41] separates three groups (Figure 11). The flat profiles (slope angles 0.6–3.4°) lie at altitudes of 15–70 m and have the lowest maximum B-horizon TREY contents (12.6–212 ppm); the moderate profiles (4.7–5.2°) lie at the highest altitudes of the dataset (80–91 m) and include the most enriched profile, B6 (575.5 ppm; 1.95 times the parent granite); and the hilly profile B5 (12.0°) contains high TREY contents inherited from its REE-rich parent but is depleted relative to it (0.76 times). The highest enrichment factors (1.10 and 1.95) therefore occur at intermediate slope angles, probably because weathering outpaces erosion there while the regolith is still drained downslope; enrichment decreases towards steeper slopes, where the upper horizons are removed by mass wasting, and towards the deposition zone, where the regolith is intensely leached and probably mixed with transported material (Section 5.5).

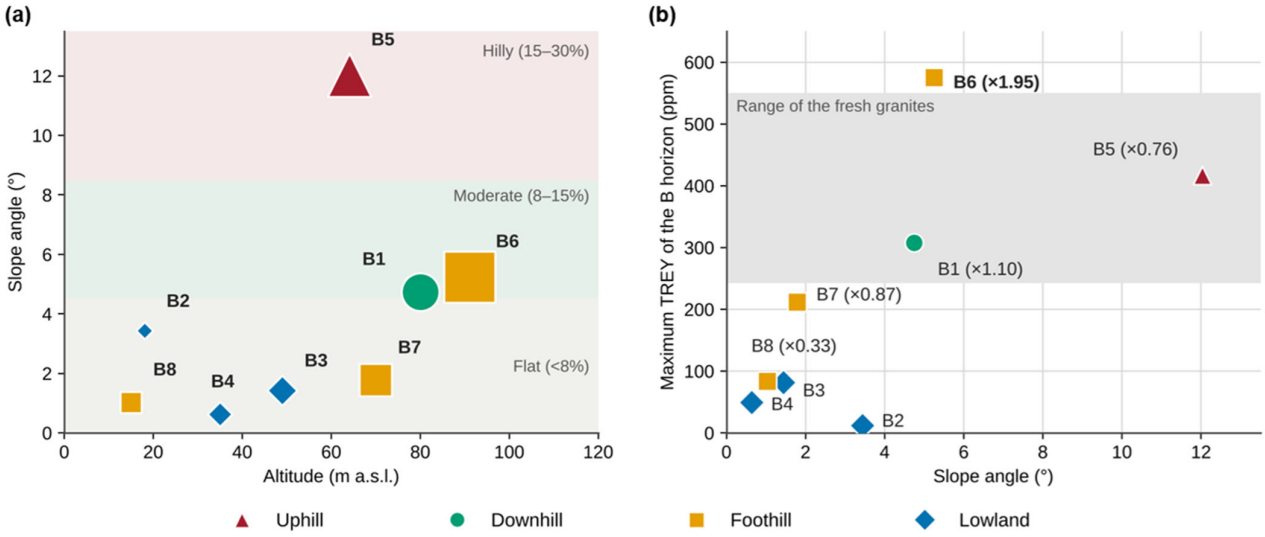


Figure 11. Numerical terrain classification of the profiles: (**a**) slope angle versus altitude [41], with symbol size proportional to the maximum TREY of the B horizon, and (**b**) maximum B-horizon TREY versus slope angle, with the enrichment factor relative to the parent granite in parentheses. The shaded bands in (**a**) are the slope classes of Section 3.1, and the grey band in (**b**) is the TREY range of the fresh granites.

The hydrographic parameters (Table 9; Figure 12) support this zonation. The slope profiles B1, B5, and B6 lie 34–58 m above the nearest drainage line (HAND) and 0.5–1.7 km (flow distance) from it, and their receiving first-order streams are among the steepest of the dataset (0.60%–1.09% over the first 2 km), with knickpoints downstream of B5 and B6; these characteristics place them in the track zone. In contrast, the lowland profiles B2–

B4 lie only 11–23 m above the drainage, and B2 lies beside the third-order Air Mangkung (catchment 18 km²), whose nearly flat (0.11%) and meandering (sinuosity 1.67) talweg is characteristic of the deposition zone. Profile B7 lies 18 m above a first-order tributary of Sungai Bakung at the foot of a granite ridge, consistent with its transitional position, and B8 drains directly to the sea, 0.27 km away and only ~9 m above sea level. The drainage pattern is radial around the granite hills (B5–B8) and dendritic to irregular in the lowlands, where numerous closed depressions interrupt the network (Figure 12c–j). The two profiles with the highest enrichment factors (B6, 1.95; B1, 1.10) also stand highest above the local drainage (56–58 m), whereas the profiles closest to the drainage base (B2–B4, B7, and B8) are REE-poor; B5, although 34 m above the drainage, lies on the steepest hillslope and is depleted. REE enrichment therefore occurs where the regolith is well drained but not eroded, i.e., on moderate lower slopes high above the talweg in the track zone.

Table 9. DEM-derived two- and three-dimensional hydrographic parameters of the profiles (Copernicus GLO-30).

Profile	Drainage Pattern (2D)	Receiving Stream: Order/Catchment (km²)	Flow Distance to Stream (m)	HAND (m)	Local Relief, 1 km (m)	Talweg Gradient (%)	Sinuosity	Knickpoints (n)	Channel Length to Coast (km)
B1	Dendritic; lower flank of a granite hill	1/1.8 (Air Batupenyaber)	1360	56	162	0.60	1.15	0	19.3
B2	Dendritic; beside a trunk stream	3/18.0 (Air Mangkung)	300	11	29	0.11	1.67	0	12.2
B3	Irregular; hummocky lowland with closed depressions	2/6.1	880	23	48	0.29	1.16	0	9.3
B4	Irregular; hummocky lowland with closed depressions	1/1.3	450	11	81	0.51	1.05	0	10.4
B5	Radial–parallel; ridge flank	1/1.0 (not mapped)	1650	34	124	0.61	1.14	2	3.9
B6	Radial; flank of a granite massif	1/1.0 (Air Gedung)	530	58	419	1.09	1.02	1	2.9
B7	Radial–dendritic; foot of a granite ridge	1/3.7 (tributary of Sungai Bakung)	1500	18	297	0.58	1.06	2	10.7
B8	Short coastal streams; small headland	– (drains to the sea)	270 (to the coast)	9 *	125	–	–	–	0.27

Receiving stream = first stream (contributing area ≥ 1 km²) reached along the D8 flow path from the profile; names from the RBI map [43]. HAND = height above the nearest drainage. Talweg gradient and horizontal sinuosity are measured over the first 2 km of the receiving stream (sinuosity on the smoothed flow path); knickpoints are counted from the profile to the coast (criteria in Section 3.4). * B8 drains directly to the sea; the value is its elevation above sea level. All values are derived from a 30 m surface model and are intended for relative comparison only.

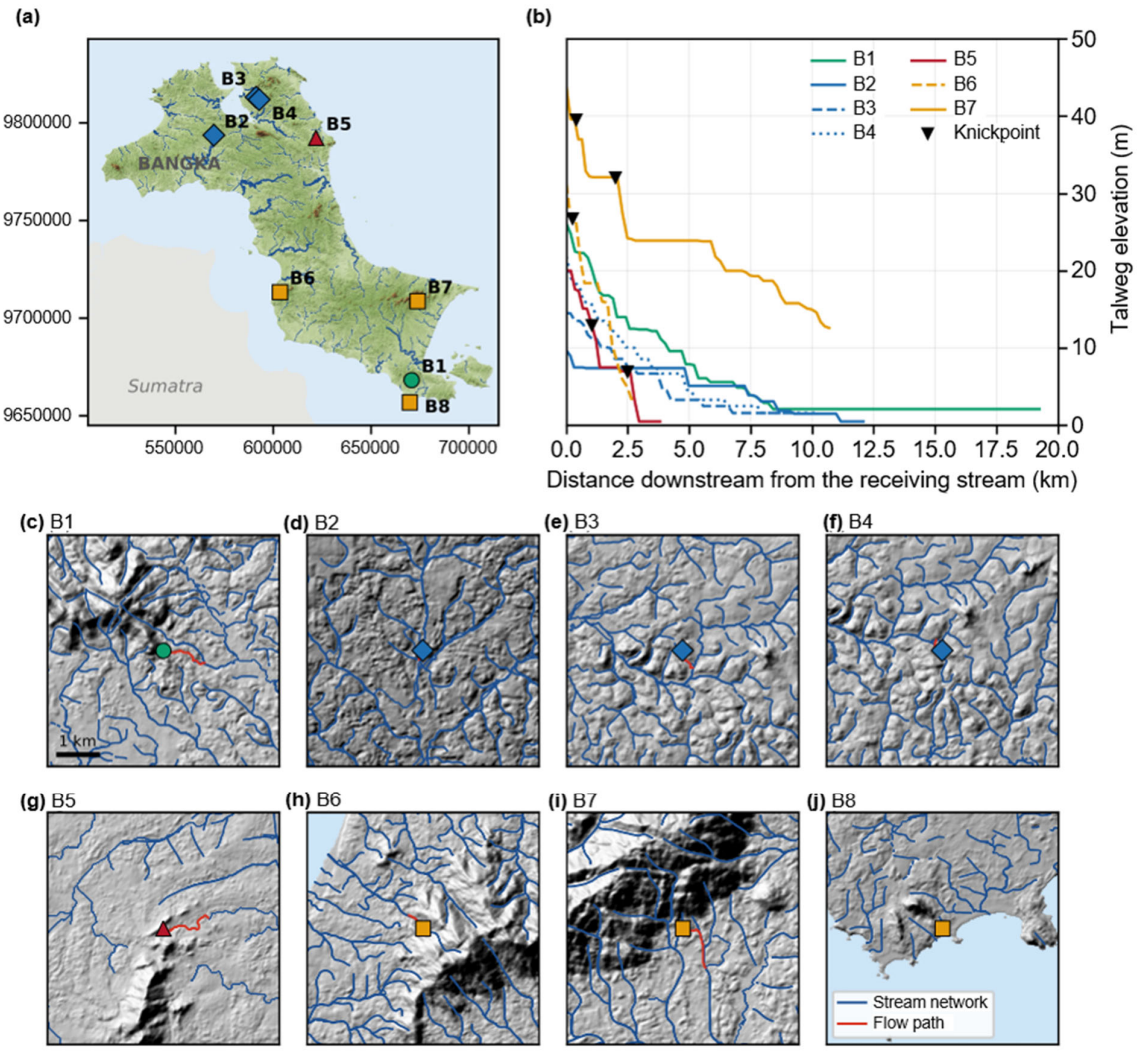


Figure 12. DEM-based hydrographic analysis of the profiles: (**a**) shaded relief and stream network of Bangka Island (blue; streams of Strahler order ≥3 derived from the Copernicus GLO-30 DEM conditioned with the RBI rivers, merged with the main rivers of the 1:50,000 RBI map [43]), with the profile locations (UTM Zone 48S; Sumatra in grey); (**b**) talweg profiles of the receiving streams from the profiles to the coast, with knickpoints; and (**c**–**j**) 6 × 6 km windows around profiles B1–B8 showing the stream network (blue; streams derived from the conditioned DEM with a contributing area ≥ 1 km², merged with the rivers of the 1:50,000 RBI map [43]) and the flow path from the profile to the receiving stream (red). Profile symbols as in Figure 11: red triangle, uphill; green circle, downhill; orange squares, foothill; blue diamonds, lowland (Table 1). Elevation data: Copernicus DEM GLO-30, © DLR e.V. 2010–2014 and © Airbus Defence and Space GmbH 2014–2018, provided under COPERNICUS by the European Union and ESA.

Four land-forming processes control this pattern. (1) Chemical weathering (etching) under the humid tropical climate deepens the regolith and releases the REE (Section 5.1). (2) Mass wasting, mainly soil creep and sheet wash, removes the upper horizons on hilly slopes, as at B5, and moves regolith and residual heavy minerals downslope towards the foothills [17]. (3) Fluvial processes incise the valleys and accumulate sediments and heavy minerals in the deposition zone, where the alluvial deposits (Qa) host the tin placers [24,25]. (4) Quaternary sea-level changes shifted the base level of the drainage systems: during glacial lowstands, the Sunda Shelf was exposed and crossed by rivers [79], which

favored valley incision and the reworking of placers, whereas the post-glacial sea-level rise flooded the shelf and the lower valleys and promoted aggradation. The regolith of the deposition zone was therefore probably reworked repeatedly, which is consistent with the mixed compositions of the lowland profiles (Section 5.5).

The terrain analysis is limited by the resolution of the elevation data. At 30 m, the D8 network does not resolve small channels, the sinuosity values are affected by the grid geometry, and the surface model includes vegetation, so that absolute elevations and short-distance gradients are uncertain; these parameters are therefore used for a relative comparison of the profiles. Higher-resolution terrain data (e.g., DEMNAS or lidar) would allow the hydrographic zones and knickpoints to be mapped in more detail.

6. Conclusions

The results of this study indicate that REE mobility and enrichment are governed by the combined influence of mineralogical, geochemical, and geomorphological factors, expressed in the redistribution of REE inherited from the parent rock, Ce anomalies, horizon mineralogy, and stable moderate slopes on lower hillslopes. Together, these factors play significant roles in the development of REE-enriched horizons within the weathered granite profiles of Bangka Island. Dickite and tourmaline in the parent granites record post-magmatic alteration at low to moderate temperatures and boron-rich hydrothermal activity, respectively. SEM–EDS identifies monazite-(Ce) and allanite-(Ce), with minor zircon and apatite, as the main REE-bearing minerals of the parent granites, and radiation damage in U–Th-bearing accessory minerals may facilitate the release of REE during weathering. Kaolinite may host adsorbed REE ions, but bulk REE contents do not correlate positively with kaolinite abundance, and whether the REE are held as exchangeable ions or in secondary or residual phases remains to be determined; where kaolinite-rich horizons remain REE-poor, the limitation appears to lie in REE supply from the parent material and in the horizon's redox conditions. According to the data, the strongest enrichment (575.5 ppm TREY, ~0.07 wt.% TREO, 1.95 times the parent granite) develops where relative elevation and stable slope gradients (8%–15%) allow complete weathering horizons to form. During weathering under stable topography, REE ions are released and mobilized into the weathered profiles. Furthermore, a negative Ce anomaly in the B horizon beneath a Ce-positive surface horizon can indicate zones of REE accumulation. However, the grades are low and LREE-dominated, and the ion-exchangeable fraction and the lateral continuity of the enriched horizon were not determined, so the economic significance of the profiles remains to be assessed. Although these indicators were derived from spatially distributed profiles and are qualitative, they offer provisional screening guides for regolith-hosted REE exploration in tropical granitic terrains, to be calibrated with ion-exchangeable REE data, grade–thickness data, and single-lithology slope sequences. Comparison with weathered granites in South Bangka suggests that the REE mineralogy of the parent granite, particularly the proportion of REE held in weathering-susceptible minerals, should be established early when similar terrains are screened. Finally, the clay and heavy minerals link the REE-enriched regolith to primary tin mineralization and placers within one granite-derived mineral system, in which REE enrichment relative to the parent granite is greatest on moderate lower slopes of the track zone, between the erosional hillslopes and the deposition zone.#

Supplementary Materials: The following supporting information can be downloaded at https://www.mdpi.com/article/10.3390/min16121241/s1: Supplementary S1 shows Table S1. Representative SEM–EDS spot analyses of REE- and Th-bearing accessory minerals in the fresh granites, with the EDS reports (SEM images and spectra): samples B1-R, B5-R, B6-R1, B6-R2, B7-R and B8-R. Supplementary S2 shows Table S2. Modal proportions of quartz, alkali feldspar, and plagioclase in

the fresh granites estimated in six fields of view per thin section, and their QAP classification: Table S2a (estimates per field of view), Table S2b (sample means and QAP classification) and the IUGS QAP fields used. Supplementary S3 shows Figure S1. (a) Total alkali–silica diagram for plutonic rocks, (b) A/NK versus ASI diagram, and (c) QAP diagram of the fresh granites.

Author Contributions: Conceptualization, P.R. and S.; Methodology, P.R. and S.; Validation, S., A.N.H.H. and A.Y.A.H.; Formal Analysis, P.R.; Investigation, P.R., S. and I.G.S.; Data Curation, P.R., S. and I.G.S.; Writing—Original Draft Preparation, P.R. and S.; Writing—Review & Editing, P.R., A.N.H.H. and I.S.; Supervision, S., A.N.H.H., A.Y.A.H. and I.S.; Funding Acquisition, S. All authors have read and agreed to the published version of the manuscript.

Funding: This research was funded by Institut Teknologi Bandung through the Program for Research, Community Service, and Innovation (PPMI 2026) with grant number 2129/IT1.C05/TA/2026, and by the Ministry of Education, Culture, Research, and Technology of the Republic of Indonesia through the Higher Education Research Program (PDUPT), grant number 007/E5/PG.02.00.PT/2022.

Data Availability Statement: The data presented in this study are available within the article and its Supplementary Materials. Further inquiries can be directed to the corresponding author.

Acknowledgments: The authors thank Institut Teknologi Bandung and the Center for Research and Technology of Nuclear Minerals, National Research and Innovation Agency, for laboratory support.

Conflicts of Interest: The authors declare no conflicts of interest.

References

1. Dushyantha, N.; Batapola, N.; Ilankoon, I.; Rohitha, S.; Premasiri, R.; Abeysinghe, B.; Ratnayake, N.P.; Dissanayake, K. The story of rare earth elements (REEs): Occurrences, global distribution, genesis, geology, mineralogy and global production. *Ore Geol. Rev.* **2020**, *122*, 103521. https://doi.org/10.1016/j.oregeorev.2020.103521.
2. Rudnick, R.L.; Gao, S. The composition of the continental crust. *Treatise Geochem.* **2003**, *3*, 1–64. https://doi.org/10.1016/B0-08-043751-6/03016-4.
3. Republic of Indonesia. Presidential Regulation No. 79 of 2023 on the Amendment to Presidential Regulation No. 55 of 2019 on the Acceleration of the Battery Electric Vehicle Program for Road Transportation. State Gazette of the Republic of Indonesia 2023 No. 154; Jakarta, Indonesia, 2023. Available online: https://jdih.kemenkeu.go.id/dok/perpres-79-tahun-2023 (accessed on 17 November 2026).
4. Sanematsu, K.; Watanabe, Y. Characteristics and genesis of ion adsorption-type rare earth element deposits. *Rev. Econ. Geol.* **2016**, *18*, 55–79. https://doi.org/10.5382/Rev.18.03.
5. Bao, Z.; Zhao, Z. Geochemistry of mineralization with exchangeable REY in the weathering crusts of granitic rocks in South China. *Ore Geol. Rev.* **2008**, *33*, 519–535. https://doi.org/10.1016/j.oregeorev.2007.03.005.
6. Li, Y.; Zhao, W.; Zhou, M. Nature of parent rocks, mineralization styles and ore genesis of regolith-hosted REE deposits in South China: An integrated genetic model. *J. Asian Earth Sci.* **2017**, *148*, 65–95. https://doi.org/10.1016/j.jseaes.2017.08.004.
7. Hoshino, M.; Sanematsu, K.; Watanabe, Y. REE mineralogy and resources. In *Handbook on the Physics and Chemistry of Rare Earths*; Elsevier: Amsterdam, The Netherlands, 2016; Volume 49, pp. 129–291. https://doi.org/10.1016/bs.hpcre.2016.03.006.
8. Gan, L.; Yan, B.; Liu, Y.; Gao, Y.; Yin, C.; Zhu, L.; Tan, S.; Ding, D.; Jiang, H. Geochemical and mineralogical characteristics of ion-adsorption type REE mineralization in the Mosuoying granite, Panxi area, Southwest China. *Minerals* **2023**, *13*, 1449. https://doi.org/10.3390/min13111449.
9. Borst, A.M.; Smith, M.P.; Finch, A.A.; Estrade, G.; de Benavent, C.V.; Nason, P.; Marquis, E.; Horsburgh, N.J.; Goodenough, K.M.; Xu, C.; et al. Adsorption of rare earth elements in regolith-hosted clay deposits. *Nat. Commun.* **2020**, *11*, 4386. https://doi.org/10.1038/s41467-020-17801-5.
10. Sergeev, N.; Collins, T. Regolith-hosted rare earth element mineralization in the Esperance region, Western Australia: Major characteristics and potential controls. *Minerals* **2024**, *14*, 847. https://doi.org/10.3390/min14080847.
11. Sanematsu, K. Resource potential of REE in Sundaland, Southeast Asia. In Proceedings of the Sundaland Resources 2014: MGEI Annual Convention, Palembang, Indonesia, 17–18 November 2014; pp. 163–180.
12. Sanematsu, K.; Kon, Y.; Imai, A. Influence of phosphate on mobility and adsorption of REEs during weathering of granites in Thailand. *J. Asian Earth Sci.* **2015**, *111*, 14–30. https://doi.org/10.1016/j.jseaes.2015.05.018.

13. Hakim, A.Y.A.; Sunjaya, D.; Hede, A.N.H.; Indriati, T.; Hidayat, T. Critical raw materials associated with the lateritic bauxite and red mud in West Kalimantan, Indonesia. *Geochem. Explor. Environ. Anal.* **2023**, *23*, geochem2022-064. https://doi.org/10.1144/geochem2022-064.
14. Sukadana, I.G.; Sulaeman; Syaeful, H.; Indrastomo, F.D.; Adimedha, T.B.; Ciputra, R.C.; Pratiwi, F.; Mustika, D.; Sumaryanto, A.; Burhannudinnur, M.; et al. High field strength element (HFSE) and rare earth element (REE) enrichment in laterite deposit of high background natural radiation area (HBNRA) of Mamuju, West Sulawesi, Indonesia. *Resources* **2025**, *14*, 84. https://doi.org/10.3390/resources14050084.
15. Schwartz, M.O.; Rajah, S.S.; Askury, A.K.; Putthapiban, P.; Djaswadi, S. The Southeast Asian tin belt. *Earth-Sci. Rev.* **1995**, *38*, 95–293. https://doi.org/10.1016/0012-8252(95)00004-T.
16. Yang, M.; Liang, X.; Ma, L.; Huang, J.; He, H.; Zhu, J. Adsorption of REEs on kaolinite and halloysite: A link to the REE distribution on clays in the weathering crust of granite. *Chem. Geol.* **2019**, *525*, 210–217. https://doi.org/10.1016/j.chemgeo.2019.07.024.
17. Li, M.Y.H.; Zhou, M.F.; Williams-Jones, A.E. Controls on the dynamics of rare earth elements during sub-tropical hillslope processes and formation of regolith-hosted deposits. *Econ. Geol.* **2020**, *115*, 1097–1118. https://doi.org/10.5382/econgeo.4727.
18. Liu, W.; Li, Y.; Wang, X.; Cui, L.; Zhao, Z.; Liu, C.; Xu, Z. Weathering stage and topographic control on rare earth element (REE) behavior: New constraints from a deeply weathered granite hill. *Chem. Geol.* **2022**, *610*, 121066. https://doi.org/10.1016/j.chemgeo.2022.121066.
19. Xia, Z.; Zhang, J.; Wu, N.; He, M.; Liu, Q.; Zhao, Z. Behavior of rare earth elements during the chemical weathering of two granite profiles in different climatic regions of southern China. *Appl. Geochem.* **2025**, *181*, 106303. https://doi.org/10.1016/j.apgeochem.2025.106303.
20. Guo, W.; Zhao, Z.; Wang, C.; Wang, D.; Chen, X.; Dang, X.; Zhang, W.; Zhao, C. Micro-topographic controls on rare earth element accumulation and fractionation in weathering profiles: Case study of ion-adsorption rare earth element deposit in Hedi, Zhejiang Province, China. *Minerals* **2024**, *14*, 1178. https://doi.org/10.3390/min14111178.
21. Fan, H.; Chen, Z.; Zeng, L.; Wu, D.; Qi, F.; Chen, Z.; Wang, T.; Wan, W.; Wang, S. Geochemical behaviors and constraints on REE enrichment in weathered crust of shallow metamorphic rocks: Insights from the Getengzui ion-adsorption REE deposit, South China. *Minerals* **2026**, *16*, 321. https://doi.org/10.3390/min16030321.
22. Ng, S.W.-P.; Whitehouse, M.J.; Roselee, M.H.; Teschner, C.; Murtadha, S.; Oliver, G.J.H.; Ghani, A.A.; Chang, S.-C. Late Triassic granites from Bangka, Indonesia: A continuation of the Main Range granite province of the South-East Asian Tin Belt. *J. Asian Earth Sci.* **2017**, *138*, 548–561. https://doi.org/10.1016/j.jseaes.2017.03.002.
23. Suharjo, E.G.W.; Takahashi, R.; Agangi, A.; Syafrizal; Manalo, P.; Nopeia, M. Apatite and biotite geochemistry constraints on the petrogenesis of the granites in Bangka Island, Indonesia: Implications for tin mineralization. *Resour. Geol.* **2025**, *75*, e70017. https://doi.org/10.1111/rge.70017.
24. Mangga, S.A.; Djamal, B. *Geological Map of the North Bangka Quadrangle, Sumatra (Scale 1:250,000)*; Geological Research and Development Centre: Bandung, Indonesia, 1994.
25. Margono, U.; Supandjono, R.J.B.; Partoyo, E. *Geological Map of the South Bangka Quadrangle, Sumatra (Scale 1:250,000)*; Geological Research and Development Centre: Bandung, Indonesia, 1995.
26. Yang, J.H.; Hu, R.Z.; Zhou, M.F.; Lehmann, B.; Zhao, J.H.; Wu, J.H.; Liu, L.; Mao, W.; Cui, Z.T.; Rosana, M.F. Cassiterite U–Pb ages from the Tin Islands, Indonesia, the southern end of the Southeast Asian tin province. *Miner. Depos.* **2025**, *60*, 1755–1767. https://doi.org/10.1007/s00126-025-01373-9.
27. Aryanto, N.C.D.; Kamiludin, U. The content of placer heavy mineral and characteristics of REE at Toboali Coast and its surrounding area, Bangka Belitung Province. *Bull. Mar. Geol.* **2016**, *31*, 45–54. https://doi.org/10.32693/bomg.31.1.2016.318.
28. Syafrizal; Hede, A.N.H.; Rivai, T.A.; Sihite, R.F. Characterization of rare earth elements in cassiterite associated minerals in Bangka-Belitung Islands, Indonesia. *Indones. J. Geosci.* **2024**, *11*, 201–219. https://doi.org/10.17014/ijog.11.2.201-219.
29. Tampubolon, A.; Syafri, I.; Rosana, M.F.; Yuningsih, E.T. Secondary enrichment of REE in weathered granite, South Bangka, Indonesia. *Indones. J. Geosci.* **2024**, *11*, 141–165. https://doi.org/10.17014/ijog.11.1.141-165.
30. Agung, Y.Z.; Watanabe, Y.; Tampubolon, A.; Purnama, A.B.; Rosana, M.F. Characteristics of REE enrichments in the weathered granitic crust, Toboali, South Bangka: Possibility for ion adsorption-type REE mineralization. *Resour. Geol.* **2024**, *74*, e12343. https://doi.org/10.1111/rge.12343.
31. Syafrizal; Rasma, P.; Hakim, A.Y.A. Potential REE-Li resources in lateritic granite in Indonesian granitoid formations: A review. *IOP Conf. Ser. Earth Environ. Sci.* **2022**, *1031*, 012032. https://doi.org/10.1088/1755-1315/1031/1/012032.
32. Yusoff, Z.; Ngwenya, B.; Parsons, I. Mobility and fractionation of REEs during deep weathering of geochemically contrasting granites in a tropical setting, Malaysia. *Chem. Geol.* **2013**, *349*, 71–86. https://doi.org/10.1016/j.chemgeo.2013.04.016.

33. Yaraghi, A.; Ariffin, K.S.; Baharun, N. Comparison of characteristics and geochemical behaviors of REEs in two weathered granitic profiles generated from metamictized bedrocks in Western Peninsular Malaysia. *J. Asian Earth Sci.* **2020**, *199*, 104385. https://doi.org/10.1016/j.jseaes.2020.104385.
34. Setiawan, I.; Takahashi, R.; Imai, A. Petrochemistry of granitoids in Sibolga and its surrounding areas, North Sumatra, Indonesia. *Resour. Geol.* **2017**, *67*, 254–278. https://doi.org/10.1111/rge.12132.
35. Lintjewas, L.; Setiawan, I. Mobility of rare earth element in hydrothermal process and weathering product: A review. *IOP Conf. Ser. Earth Environ. Sci.* **2018**, *118*, 012076. https://doi.org/10.1088/1755-1315/118/1/012076.
36. Syafrizal; Hede, A.N.H.; Hakim, A.Y.A.; Permatasari, M.I. Identifikasi keberadaan rare earth elements tipe ion adsorption pada lempung: Sampel dari Muntok dan Lubuk Besar, Pulau Bangka. *J. GEOSAPTA* **2021**, *7*, 125–132. https://doi.org/10.20527/jg.v7i2.10897.
37. USDA Natural Resources Conservation Service. Available online: https://www.nrcs.usda.gov/ (accessed on 6 October 2026).
38. Syafrizal; Hede, A.N.H.; Hakim, A.Y.A.; Sihite, R.F. Karakterisasi mineral ikutan timah pembawa REE di Bangka Selatan dan Badau, Provinsi Kepulauan Bangka Belitung. *J. GEOSAPTA* **2021**, *7*, 7–13. https://doi.org/10.20527/jg.v7i1.8652.
39. Flude, S.; Haschke, M.; Storey, M. Application of benchtop micro-XRF to geological materials. *Mineral. Mag.* **2017**, *81*, 923–948. https://doi.org/10.1180/minmag.2016.080.150.
40. Nesbitt, H.W.; Young, G.M. Early Proterozoic climates and plate motions inferred from major element chemistry of lutites. *Nature* **1982**, *299*, 715–717. https://doi.org/10.1038/299715a0.
41. Dill, H.G.; Buzatu, A.; Balaban, S.-I.; Kleyer, C. Compositional and numerical geomorphology along a basement–foreland transition, SE Germany, with special reference to landscape-forming indices and parameters in genetic and applied terrain analyses. *Geosciences* **2025**, *15*, 37. https://doi.org/10.3390/geosciences15020037.
42. European Space Agency. Copernicus Digital Elevation Model GLO-30. Available online: https://copernicus-dem-30m.s3.amazonaws.com (accessed on 17 November 2026).
43. Geospatial Information Agency of Indonesia (BIG). *Rupabumi Indonesia (RBI) Topographic Map, Scale 1:50,000, Kepulauan Bangka Belitung Province (Edition 2022)*; BIG: Cibinong, Indonesia, 2022. Available online: https://tanahair.indonesia.go.id (accessed on 17 November 2026).
44. Lindsay, J.B. The practice of DEM stream burning revisited. *Earth Surf. Process. Landf.* **2016**, *41*, 658–668. https://doi.org/10.1002/esp.3888.
45. O'Callaghan, J.F.; Mark, D.M. The extraction of drainage networks from digital elevation data. *Comput. Vis. Graph. Image Process.* **1984**, *28*, 323–344. https://doi.org/10.1016/S0734-189X(84)80011-0.
46. Strahler, A.N. Quantitative analysis of watershed geomorphology. *Trans. Am. Geophys. Union* **1957**, *38*, 913–920. https://doi.org/10.1029/TR038i006p00913.
47. Rennó, C.D.; Nobre, A.D.; Cuartas, L.A.; Soares, J.V.; Hodnett, M.G.; Tomasella, J.; Waterloo, M.J. HAND, a new terrain descriptor using SRTM-DEM: Mapping terra-firme rainforest environments in Amazonia. *Remote Sens. Environ.* **2008**, *112*, 3469–3481. https://doi.org/10.1016/j.rse.2008.03.018.
48. Ehrenberg, S.N.; Aagaard, P.; Wilson, M.J.; Fraser, A.R.; Duthie, D.M.L. Depth-dependent transformation of kaolinite to dickite in sandstones of the Norwegian continental shelf. *Clay Miner.* **1993**, *28*, 325–352. https://doi.org/10.1180/claymin.1993.028.3.01.
49. Beaufort, D.; Cassagnabère, A.; Petit, S.; Lanson, B.; Berger, G.; Lacharpagne, J.C.; Johansen, H. Kaolinite-to-dickite reaction in sandstone reservoirs. *Clay Miner.* **1998**, *33*, 297–316. https://doi.org/10.1180/000985598545499.
50. Fialips, C.; Majzlan, J.; Beaufort, D.; Navrotsky, A. New thermochemical evidence on the stability of dickite vs. kaolinite. *Am. Mineral.* **2003**, *88*, 837–845. https://doi.org/10.2138/am-2003-5-612.
51. Wu, H.H.; Huang, H.; Zhang, Z.C.; Yang, S.; Gao, Y.; Finch, A.A. Tourmaline chemical and boron isotopic constraints on the magmatic-hydrothermal transition and rare-metal mineralization in alkali granitic systems. *Am. Mineral.* **2024**, *109*, 1461–1477. https://doi.org/10.2138/am-2023-9131.
52. Moore, D.M.; Reynolds, R.C., Jr. *X-Ray Diffraction and the Identification and Analysis of Clay Minerals*, 2nd ed.; Oxford University Press: Oxford, UK, 1997.
53. Churchman, G.J.; Whitton, J.S.; Claridge, G.G.C.; Theng, B.K.G. Intercalation method using formamide for differentiating halloysite from kaolinite. *Clays Clay Miner.* **1984**, *32*, 241–248. https://doi.org/10.1346/CCMN.1984.0320401.
54. Jaiswal, A.; Banerjee, S.; Mani, R.; Chattopadhyaya, M.C. Synthesis, characterization and application of goethite mineral as an adsorbent. *J. Environ. Chem. Eng.* **2013**, *1*, 281–289. https://doi.org/10.1016/j.jece.2013.05.007.
55. Rollinson, H.R. *Using Geochemical Data: Evaluation, Presentation, Interpretation*; Routledge: London, UK, 1993.

56. Chappell, B.W.; White, A.J.R. Two contrasting granite types: 25 years later. *Aust. J. Earth Sci.* **2001**, *48*, 489–499. https://doi.org/10.1046/j.1440-0952.2001.00882.x.
57. Frost, B.R.; Barnes, C.G.; Collins, W.J.; Arculus, R.J.; Ellis, D.J.; Frost, C.D. A geochemical classification for granitic rocks. *J. Petrol.* **2001**, *42*, 2033–2048. https://doi.org/10.1093/petrology/42.11.2033.
58. Crow, M.J.; van Leeuwen, T.M. Metallic mineral deposits. In *Sumatra: Geology, Resources and Tectonic Evolution*; Barber, A.J., Crow, M.J., Milsom, J.S., Eds.; Geological Society Memoir 31; Geological Society: London, UK, 2005; pp. 147–174. https://doi.org/10.1144/GSL.MEM.2005.031.01.12.
59. Middlemost, E.A.K. Naming materials in the magma/igneous rock system. *Earth-Sci. Rev.* **1994**, *37*, 215–224. https://doi.org/10.1016/0012-8252(94)90029-9.
60. Le Maitre, R.W. *Igneous Rocks: A Classification and Glossary of Terms*; Cambridge University Press: Cambridge, UK, 2002.
61. Streckeisen, A. To each plutonic rock its proper name. *Earth-Sci. Rev.* **1976**, *12*, 1–33. https://doi.org/10.1016/0012-8252(76)90052-0.
62. Pérez-Soba, C.; Villaseca, C. Li-Na-metasomatism related to I-type granite magmatism: A case study of the highly fractionated La Pedriza pluton (Iberian Variscan belt). *Lithos* **2019**, *344–345*, 159–174. https://doi.org/10.1016/j.lithos.2019.06.008.
63. Zhao, X.; Li, N.; Smith, M.; Tan, S.; Fu, R.; Yang, Y.; Niu, H. Progressive enrichment of rare earth elements (REE) between parent granites and weathering crust contributed to the generation of regolith-hosted REE deposits in South China. *Geol. Soc. Am. Bull.* **2025**, *137*, 4516–4532. https://doi.org/10.1130/B38051.1.
64. Guo, L.; Xiong, S.; Mills, B.J.W.; Isson, T.; Yang, S.; Cui, J.; Wang, Y.; Jiang, L.; Xu, Z.; Cai, C.; et al. Acceleration of phosphorus weathering under warm climates. *Sci. Adv.* **2024**, *10*, eadm7773. https://doi.org/10.1126/sciadv.adm7773.
65. Fu, H.; Jian, X.; Pan, H. Bias in sediment chemical weathering intensity evaluation: A numerical simulation study. *Earth-Sci. Rev.* **2023**, *246*, 104574. https://doi.org/10.1016/j.earscirev.2023.104574.
66. Sun, S.S.; McDonough, W.F. Chemical and isotopic systematics of oceanic basalts: Implications for mantle composition and processes. In *Magmatism in the Ocean Basins*; Saunders, A.D., Norry, M.J., Eds.; Geological Society Special Publication 42; Geological Society: London, UK, 1989; pp. 313–345. https://doi.org/10.1144/GSL.SP.1989.042.01.19.
67. Taylor, S.R.; McLennan, S.M. The geochemical evolution of the continental crust. *Rev. Geophys.* **1995**, *33*, 241–265. https://doi.org/10.1029/95RG00262.
68. Wu, Z.; Liu, J.; Li, C.; Liu, W.; Wu, W. Redistribution and enhanced bioavailability of rare earth elements speciation induced by mining-driven transformation in ionic rare earth mining areas. *Sci. Rep.* **2025**, *15*, 27345. https://doi.org/10.1038/s41598-025-13513-2.
69. Sanematsu, K.; Kon, Y.; Imai, A.; Watanabe, K.; Watanabe, Y. Geochemical and mineralogical characteristics of ion-adsorption type REE mineralization in Phuket, Thailand. *Miner. Depos.* **2013**, *48*, 437–451. https://doi.org/10.1007/s00126-011-0380-5.
70. Dostal, J. Rare earth element deposits of alkaline igneous rocks. *Resources* **2017**, *6*, 34. https://doi.org/10.3390/resources6030034.
71. Ishihara, S.; Hua, R.; Hoshino, M.; Murakami, H. REE abundance and REE minerals in granitic rocks in the Nanling Range, Jiangxi Province, Southern China, and generation of the REE-rich weathered crust deposits. *Resour. Geol.* **2008**, *58*, 355–372. https://doi.org/10.1111/j.1751-3928.2008.00070.x.
72. Wang, Y.; Jia, R.; Li, Y.; Yang, K.; Cui, J.; Shan, Y. Study on the mechanical properties and microscopic evolution mechanisms of weathered granite soil. *Sci. Rep.* **2024**, *14*, 24388. https://doi.org/10.1038/s41598-024-75092-y.
73. Fu, W.; Li, X.; Feng, Y.; Feng, M.; Peng, Z.; Yu, H.; Lin, H. Chemical weathering of S-type granite and formation of rare earth element (REE)-rich regolith in South China: Critical control of lithology. *Chem. Geol.* **2019**, *520*, 33–51. https://doi.org/10.1016/j.chemgeo.2019.05.006.
74. Fu, W.; Luo, P.; Hu, Z.; Feng, Y.; Liu, L.; Yang, J.; Feng, M.; Yu, H.; Zhou, Y. Enrichment of ion-exchangeable rare earth elements by felsic volcanic rock weathering in South China: Genetic mechanism and formation preference. *Ore Geol. Rev.* **2019**, *114*, 103120. https://doi.org/10.1016/j.oregeorev.2019.103120.
75. Sobri, N.A.; Yunus, M.Y.B.M.; Harun, N. A review of ion adsorption clay as a high potential source of rare earth minerals in Malaysia. *Mater. Today Proc.* **2023**. https://doi.org/10.1016/j.matpr.2023.03.513.#
76. Santana, I.V.; Wall, F.; Botelho, N.F. Occurrence and behavior of monazite-(Ce) and xenotime-(Y) in detrital and saprolitic environments related to the Serra Dourada granite, Goiás/Tocantins State, Brazil: Potential for REE deposits. *J. Geochem. Explor.* **2015**, *155*, 1–13. https://doi.org/10.1016/j.gexplo.2015.03.007.
77. Wang, D.; Zhao, Z.; Yu, Y.; Dai, J.; Deng, M.; Zhao, T.; Liu, L. Exploration and research progress on ion-adsorption type REE deposit in South China. *China Geol.* **2018**, *1*, 414–423. https://doi.org/10.31035/cg2018022.

78. Estrade, G.; Marquis, E.; Smith, M.; Goodenough, K.; Nason, P. REE concentration processes in ion adsorption deposits: Evidence from the Ambohimirahavavy alkaline complex in Madagascar. *Ore Geol. Rev.* **2019**, *112*, 103027. https://doi.org/10.1016/j.oregeorev.2019.103027.
79. Voris, H.K. Maps of Pleistocene sea levels in Southeast Asia: Shorelines, river systems and time durations. *J. Biogeogr.* **2000**, *27*, 1153–1167. https://doi.org/10.1046/j.1365-2699.2000.00489.x.
80. Dill, H.G.; Buzatu, A.; Balaban, S.-I.; Rüsenberg, K.A. A mineralogical-geomorphological terrain analysis of hotspot volcanic islands—The missing link between carbonatite- and pegmatite Nb-F-Zr-Li-Be-bearing REE deposits and new tools for their exploration (Canary Islands Archipelago, Spain). *Ore Geol. Rev.* **2023**, *163*, 105702. https://doi.org/10.1016/j.oregeorev.2023.105702.

Disclaimer/Publisher's Note: The statements, opinions and data contained in all publications are solely those of the individual author(s) and contributor(s) and not of MDPI and/or the editor(s). MDPI and/or the editor(s) disclaim responsibility for any injury to people or property resulting from any ideas, methods, instructions or products referred to in the content.